The Joint International Conferences

Smart Materials and Surfaces
SMS 2019

NanoMedicine International Conference
NanoMed 2019

Oct 23 to 25, 2019, Lisbon - Italy

Conference Proceedings

DOI: https://doi.org/10.26799/cp-sms-nanomed-egf2019

Proceedings of the Joint SMS / NanoMed / EGF 2019 International Conference
Lisbon, Portugal – October 23 – 25, 2019
DOI: https://doi.org/10.26799/cp-sms-nanomed-egf2019

Modelling and Probing of Electronic Structure and Molecular Dynamics in Subchondral Femoral Bone Tissue in Intact and Damaged Areas

X.O. Brykalova[1], A.S. Konashuk[1], S.S. Sakhonenkov[1], D.O. Samoilenko[1], A.A. Cherny[2], Yu.A. Rykov[2], N.N. Kornilov[2], E.O. Filatova[1], E. Rühl[3], A.A. Pavlychev[1*]
[1] St.Petersburg State University, Department of Physics, Peterhof, Saint Petersburg, RF.
[*]andrey.pavlychev@gmail.com
[2] Vreden Russian Research Institute of Traumatology and Orthopedics,
Saint Petersburg, RF
[3] Physikalische und Theoretische Chemie, Institut für Chemie und Biochemie, Freie Universität Berlin,
Takustr. 3, 14195 Berlin, Germany

Abstract

X-ray absorption, photoelectron and Raman spectroscopic techniques are used to investigate relationships between hierarchical organization of the skeleton and local electronic and atomic structure of femoral bone in knee compartments and to understand the osteoarthritic (OA) related changes in the structure. As samples the medial and lateral condyles of the femur resected during total knee arthroplasty in patients with medial compartmental knee osteoarthritis were used. Site-dependence of the O $1s^{-1}$ and P $2p^{-1}$ photoelectron line shapes, Ca 2p near edge X-ray absorption fine structure and Raman shifts is revealed. It indicates on essential OA-related changes in electronic and atomic structure and molecular architecture and dynamics in subchondral femoral bone. Differences between the spectroscopic characteristics of core and valence excited healthy and pathology damaged bone are examined within the 3DSL model. Perspectives for development of novel methods for medical imaging and diagnosis of subchondral bone at subcellular level are discussed.

Keywords: hierarchical matter, electronic and atomic structure of bone, binding energy, osteoarthritis, XPS, NEXAPS

1. Introduction

Bone is the most complex hierarchically organized material in nature. Its complicity is determined by two strongly interacting hierarchical organizations. Both the organic and mineral organization includes seven hierarchical levels going from atoms to the skeleton and even higher to ecological spheres [1]. As a consequence of such assembling macroscopic distortions induce changes in electronic and atomic structure of bone tissue and, in contrast, changes in elemental composition and molecular architecture lead to macroscopic deviations in bone tissue. Nanolevel studies encounter great difficulty mainly because electronic and atomic structure and molecular architecture of bone nanoelements is not fully understood. This gap prevents successful solutions of many fundamental and clinically relevant problems such as the development of new methods of medical imaging at subcellular levels and medical diagnosis of skeletal pathology at the early stage.
In the world osteoarthritis (OA) is the fourth most common cause of hospitalization. Annual costs, associated only with medical care (51%) and a decrease in productivity (49%), range from 3.4 up to $ 60 billion [10]. The morphological models [2-9] based on concepts of the structural and functional organization of the skeleton in the normal and pathological conditions describe peculiarities of skeletal structural organization and its functional properties. However, the qualitative character of the models does not allow their quantitative application to OA-related changes in bone at the nanoscale. Elaboration of quantitative ex- and in-vivo models of native bone and application of modern experimental techniques is a prospective way to develop new methods of medical imaging and medical diagnosis of skeletal pathology at the early stage.
Recently, by using X-ray diffraction and X-ray photoelectron spectroscopy the substantial changes in crystallinity and chemical bonds in OA damaged knee compartments have been revealed [11]. To rationalize the emergent properties of bone matter the 3D super lattice model (3DSL) model was suggested in the work [12]. This model takes into account the structure-functional organization of the skeleton and the peculiarities of electron waves propagation in 3D superlattice assembled from the nanocrystallites of hydroxyapatite $Ca_{10}(PO_4)_6(OH)_2$ (HAP).

DOI: https://doi.org/10.26799/cp-sms-nanomed-egf2019

In the work site-dependent changes in O $1s^{-1}$ and P $2p^{-1}$ photoelectron lines, Ca 2p near edge X-ray absorption fine structure and Raman shifts in intact and OA damaged areas of subchondral femoral bone are measured and examined. Our main objective is to document the nanoscopic changes. Below, in Sect.4.1 we present the O $1s^{-1}$ and P $2p^{-1}$ photoelectron spectra measured for the distal side of the saw cuts and for the proximal side in intact and sclerotic areas as well as in the vicinities of the sclerotic area. In section 4.2 the Ca 2p NEXAFS spectra of femoral bone in the different areas are also shown and discussed. The Raman spectra of femoral bone in intact and sclerotic areas are obtained to characterize the OA-related changes in molecular architecture and dynamics in knee compartments.

2. 3DSL-Modelling

The 3DSL model suggested in [12] gives a key for understanding of basic relationships between hierarchical organization of the skeleton and local electronic and atomic structure of mineralized bone. According to [12] the effective nanocrystallite can be presented as a rectangular block with dimensions $\langle L_x \rangle \times \langle L_y \rangle \times \langle L_z \rangle \approx$ 20×7,5×3,5 nm^3.

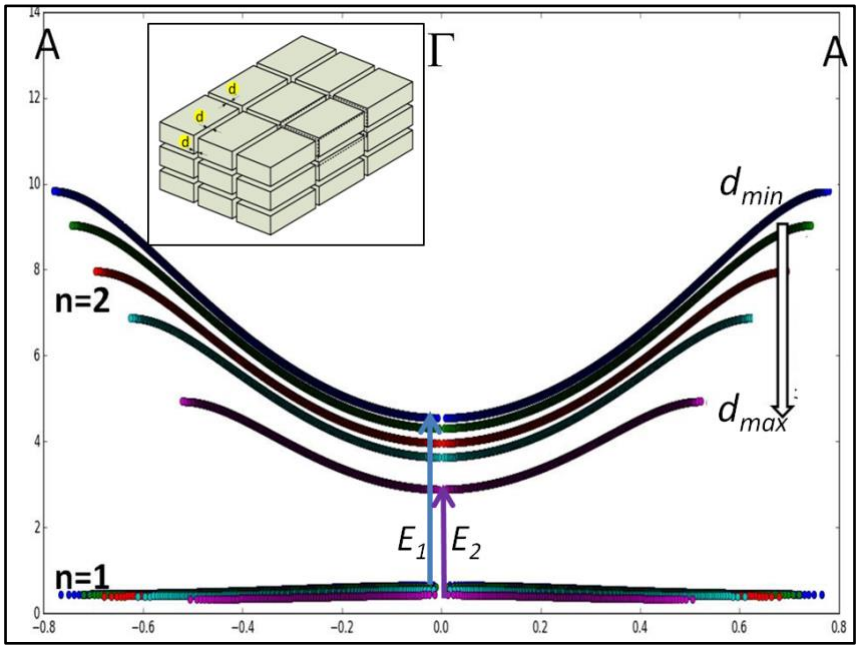

Fig. 1: Model calculations of the dispersion $E_n(k)$ of *n*-band in the superlattice as a function of the hydrated nanolayer ***d***. E_1 and E_2 are the energies of the core-to-valence interband transitions, referring to the minimal d_{min} and maximal d_{max} separation of the effective nanocrystallites. Insert: the coplanar assemble of the effective HAP-nanocrystallites separated by the nanolayers with the thickness ***d***.

It contains about $40 \cdot 10^3$ atoms. The blocks are separated one from other by the hydrated layer with the thickness $\boldsymbol{d} \approx 2$ nm. The coplanar assembly of the diverse crystallites is described as a superperiodic lattice with the basic vectors of translation $\mathbf{b}_j = \mathbf{L}_j + \boldsymbol{d}$, where $\mathbf{L}_j = \langle L_j \rangle \vec{j}$ and $\vec{j}$ is the unit vector in Cartesian coordinates. Considering the HAP-crystallite as an extended crystallographic cell derived in such a way that their coplanar assembly would form a single-crystal HAP in case the separating layers disappear (see, Insert, Fig. 1). In the assumptions the electronic structure of the 3D superlattice is approaching to the band structure of HAP when $\langle d \rangle \rightarrow 0$. This approximation is a suitable platform for investigations of the emergent HAP-to-bone deviations.
According to the 3DSL model the band structure of mineralized bone in intrafibrilar region obeys the Heine equation [12, 13]

$$X_j^2(k) - 2Z(E)X_j(k) + 1 = 0\,. \qquad (1)$$

DOI: https://doi.org/10.26799/cp-sms-nanomed-egf2019

Eq. 1 assigns the certain energy E with the wave number k where $X_j(k) \equiv e^{i\vec{k}\vec{b}_j}$. The coefficient $Z(E) = \mathrm{Re}(T(E;d,L_j))^{-1}$ links the band dispersion $E(k)$ with the short-, long-range and super-order parameters of mineralized bone, Solving Eq.1 the distinct HAP-to-bone spectral changes in the dispersion of valence band and the inter-band transitions can be revealed. Fig.1 shows the changes in energy position E_n of core (n=1) and valence (n=2) bands as a function of $\boldsymbol{d}$ are computed. The nanolayer is described as empty space. The computed results in Fig.1 show the downward shift of the bands with the increase of thickness from $\boldsymbol{d}_{min}$ to $\boldsymbol{d}_{max}$. The energy E of the inter-band transitions as a function of $\boldsymbol{d}$ is also computed. One may see that $E(\boldsymbol{d}_{min}) > E(\boldsymbol{d}_{max})$. These model results confirm the HAP-to-bone red shift predicted in [12]. They are also supported by the recent X-ray absorption spectroscopic measurements of young, adult and mature bone tissues and HAP [14]. Fig.1 also shows that

$$|\delta E_{n=1}| << \delta E_{n=2} \approx 2E_{n=2}g \qquad (2)$$

where g is the geometric factor equal to the ratio of the thickness d to the average size of the nanocrystallites in bone. We emphasize that the HAP-to-bone shift comes to nil in interfibrilar region of bone because of disordering of HAP crystallites in it. The 3DSL model also predicts the downward shift of the core and valence bands due to the dielectric shielding in the hydrated nanolevels. The band dispersion in Fig. 1 is computed by neglecting the shielding effect on transmission of electron waves in bone tissue.

3. Samples and materials

As samples of femoral bone in intact and damaged areas the medial and lateral condyles of the femur resected during total knee arthroplasty in patients with medial compartmental knee OA are used. The bone sample of damaged bone is a saw cut of the femoral condyle, subjected to excessive mechanical stress due to the development of arthritis and deformity in the joint, with full-layer loss of cartilage. The sample of healthy bone is a saw cut of the condyle of the same femoral bone, not subjected to excessive load, with intact cartilage.
The bone saw cuts were cleaned of cartilage tissue using a gentle mechanical treatment with a scalpel, to subchondral bone plate. Then, to degrease the cuts and delete the myeloid contents from the trabeculae of the spongy layer, the samples were kept for 4 days in a bath with an aqueous 33% hydrogen peroxide solution (H_2O_2) mixed in a 1:1 ratio with hot water (60° C) and with the addition of 5 ml of 10% aqueous ammonium hydroxide solution (NH_4OH). This mixture was replaced daily. To complete the cleaning process the samples were placed for one day in distilled water, changing it every 6 hours. To depress the intercrystallite water evaporation the samples were subjected to heating at 200°C for 2 days in thermostat.
Powdered bone and synthetic HAP samples were used as objects. The HAP of almost stoichiometric composition (a = 9.416 (2), c = 6.880 (1)) was synthesized by applying the reverse precipitation method in an ammonium-containing solution as it is described in [13].

4. Characterization

The X-ray photoelectron (XPS), near edge X-ray absorption (NEXAFS) and Raman (RS) spectroscopic studies are used for characterisation of local electronic and atomic structure and molecular architecture of femoral bone in OA damaged knee compartments.

4.1. XPS

The measured O $1s^{-1}$ and P $2p^{-1}$ PE lines in healthy and sclerotic areas of subchondral femoral bone as well as in the vicinities of the sclerotic area are plotted in Fig. 2. The reference XPS spectra of HAP are also shown just for comparison. The XPS spectra are measured by using the photoelectron spectrometer Thermo Fisher Scientific Escalab 250Xi.
The O $1s^{-1}$ and P $2p^{-1}$ PE line shapes in Fig. 2 make evident their strong site dependence. The XPS signals measured for the sclerotic area and outside it demonstrate substantial deviations from those referring to HAP and healthy bone. It is clear visible the appearance of a shoulder from the high binding energy side of the O $1s^{-1}$ lines registered inside and outside the sclerosis area. We note this shoulder does not appear in the spectra of HAP and healthy bone. Another shoulder arises on the low-binding-energy-side of the P $2p^{-1}$ PE line referring to the region located outside the sclerotic area. These observations agree with the basic conclusion followed from the analysis

DOI: https://doi.org/10.26799/cp-sms-nanomed-egf2019

of the Ca $2p_{3/2}^{-1}$ and Ca $2p_{1/2}^{-1}$ PE spectra of healthy and OA damaged femoral bones [11]. According to the work the "apatitic" Ca^{2+} bonds dominate in healthy bone [15]. But their contribution drops inside and outside the sclerotic area. Specifically the non-apatitic bonds demonstrate huge enhancement in the vicinities of the sclerotic area [15]. Our analysis of the O $1s^{-1}$ and P $2p^{-1}$ PE lines indicates the similar behavior of phosphorous and oxygen atoms on surface of the areas. The unambiguous assignment of the non-apatitic contributions to the O $1s^{-1}$ and P $2p^{-1}$ PE lines in OA damaged areas needs further investigations.

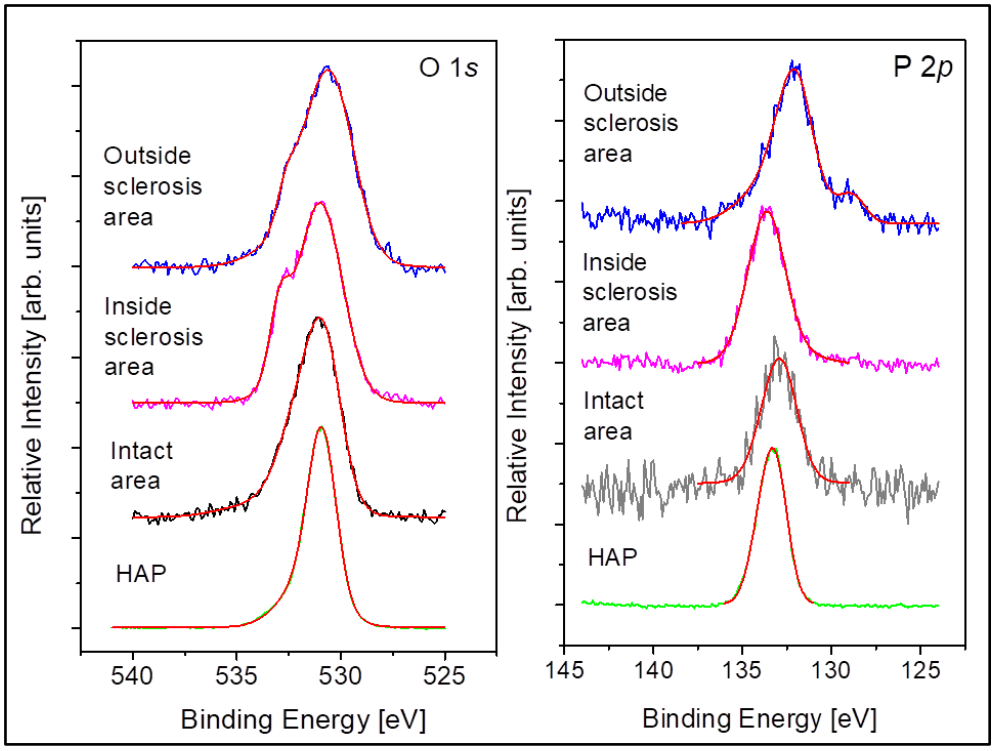

Fig. 2: O $1s^{-1}$ and P $2p^{-1}$ PE lines in HAP (bottom), intact and sclerosis areas of subchondral femoral bone and outside the sclerosis area. The best fitting results for the experimental spectra are shown with solid lines.

4.2. NEXAFS

For the first time the Ca 2p NEXAFS spectra of subchondral femoral bone are measured for the proximal side in intact and sclerotic areas as well in the vicinities of the sclerotic area. These spectra are plotted in Fig. 3. In the figure we also present the Ca 2p NEXAFS spectra of trabecular femoral bone located on the distal side of the saw cuts. The NEXAFS in Fig. 3 is mainly originated from the multiplet splitting of the Ca^{2+} $2p^5 3d^1$ excited state in the surrounding bone potential. These spectra differ from those obtained for cortical bone and discussed rather in detail in [15]. In particular, the minor HAP-to-bone red shift of the 3d bands is observed in subchondral bone. The difference supports the assignment of the HAP-to-cortex red shifts ≤0.3 eV with the superperiodic structure of mineralized plates in intrafibrilar regions [12]. The studies show that the electronic and atomic structures differ in cortical and subchondral bone tissues as well as in healthy and OA damaged areas. This allows us to suggest that the X-ray spectroscopic methods are a precision tool for imaging bone tissue at the subcellular level.

DOI: https://doi.org/10.26799/cp-sms-nanomed-egf2019

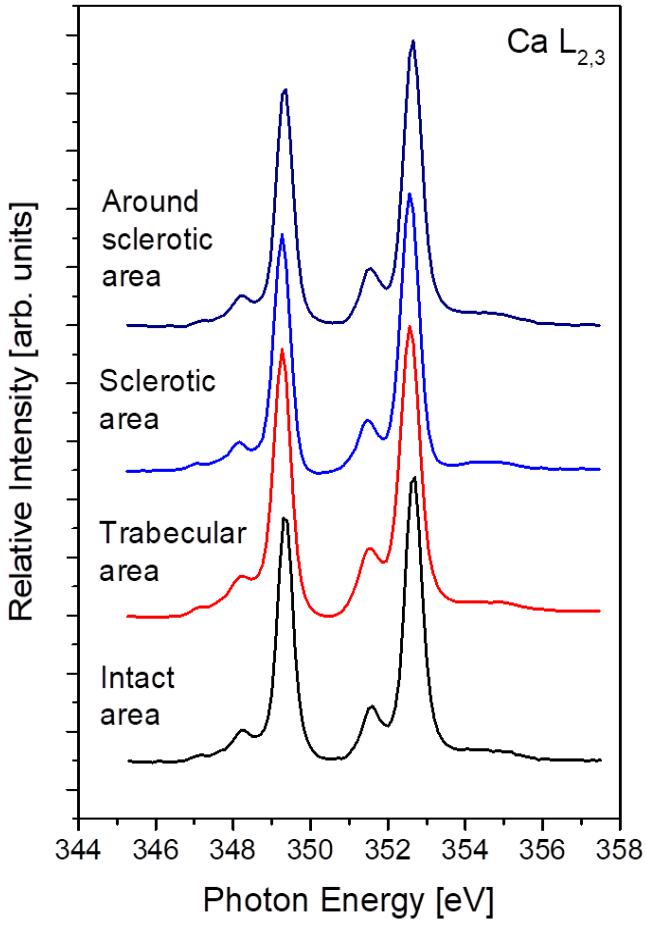

Fig. 3 Experimental X-ray absorption spectra measured near the Ca $L_{2,3}$ edges in intact, trabecular and sclerotic areas as well as around of the sclerotic area of subchondral femoral bone.

4.3 Raman

Raman microspectroscopy is applied here to specify the peculiarities of molecular architecture and dynamics in intact and sclerotic areas of subchondral bone. The Raman spectra of the bone samples are measured by using an optical microscope Olympus BX 41. Raman transitions are excited by a 532 nm cw-laser Millennia, Spectra Physics (see, for detail [16]). The measurement conditions were mild enough to preserve the bone matter from degradation under laser irradiation.

General view on Raman spectra of subchondral femoral bone in intact (red) and sclerosis (black) areas are inserted in Fig.4. Their analysis shows that the spectral changes are observed in the mineral, organic and water subsystems. As an illustration, the Raman transitions within the interval 1150 - 2000 cm^{-1} referring mainly to organic subsystem. These spectra are normalized to the most intense ν_1 PO_4 peak at 959 cm^{-1}. It can be seen that the Raman spectrum in sclerosis area is depleted in comparison with that of in intact area of subchondral bone. In particular, in sclerotic bone the transitions in at 1725 cm^{-1} and 1303 cm^{-1} are strongly depressed. This observation is consistent with the assumption [15] about the important role of chemical interaction at the border of erased cartilage with HAP crystallites in forming of AO related changes in the electron and atomic structure of subchondral femoral bone tissue.

DOI: https://doi.org/10.26799/cp-sms-nanomed-egf2019

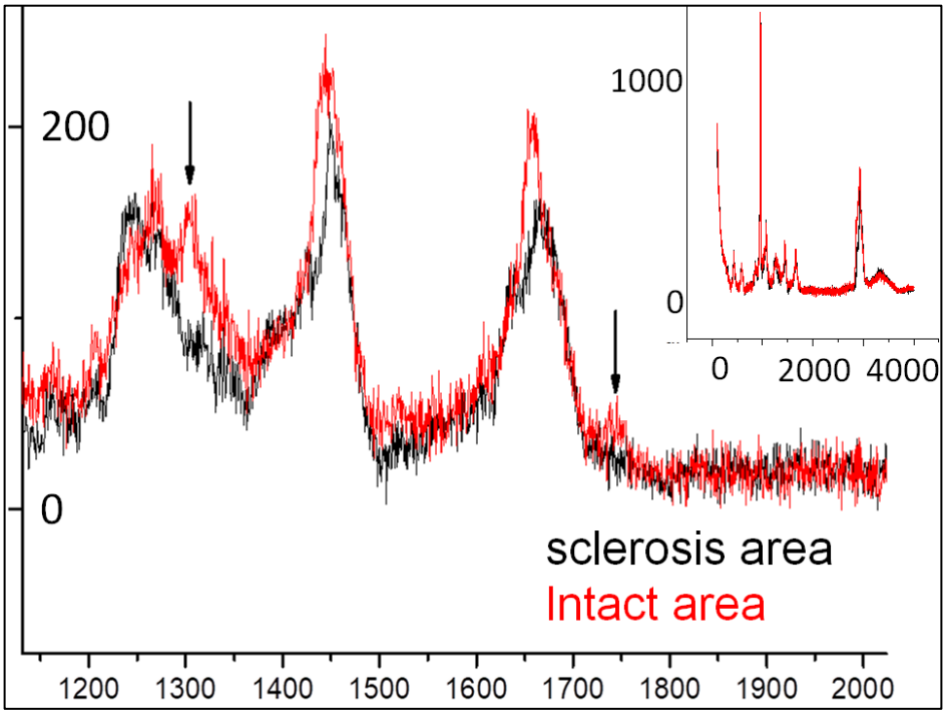

Fig. 4. Raman spectra of subchondral femoral bone in intact (red) and sclerotic (black) areas, respectively. The insert gives a general view. Raman transitions in the interval 1150 - 2000 cm^{-1} are shown on an enlarged scale. This interval refers mainly to the transitions in collagen subsystem. The spectra are normalized to the most intense ν_1 PO_4 peak at 959 cm^{-1}.

5. Conclusion

Summarizing the study we note that the 3DSL model gives us a key for understanding relationships between hierarchical organization of bone tissue and the local electronic structure of the mineralized phase and spectral distribution of oscillator strength for core-to-valence transitions in it. X-ray and Raman spectroscopic studies provide a sensitive probing of changes in electronic and atomic structure as well as molecular architecture and dynamics in healthy and OA damaged areas of subchondral femoral bone tissue. Site-dependence of the O $1s^{-1}$ and P $2p^{-1}$ photoelectron line shapes, Ca 2p near edge X-ray absorption fine structure and Raman shifts is revealed. The experimental and theoretical results show the prospects of the joint use of these spectroscopic methods for developing novel approaches to medical imaging and diagnosis of bone tissue at subcellular level and innovational technologies in medical treatment.

Acknowledgements

The XPS study was carried out with the support of the St. Petersburg State University Resource Centres “Centre for Physical Methods of Surface Investigation”, and “Centre for Diagnostics of Functional Materials for Medicine, Pharmacology and Nanoelectronics”. We gratefully acknowledge the Elettra-sincrotron-Trieste lightsource for the allocation of synchrotron radiation beamtime under proposal number 20190290.The work is supported by RFBR grant number 19-02-00891

References

1. D. Pumain, *Hierarchy in Natural and Social Sciences*, New York: Springer-Verlag, 2006.
2. W.F. Neuman and M.W. Neuman, *The chemical dynamics of bone mineral*, Chicago: University of Chicago Press, 1958.
3. J. Currey, *The mechanical adaptation of bones*, Princeton, NJ: Princeton University Press, 1984.
4. S. Weiner and H.D. Wagner, “The material bone: Structure-mechanical function relations”, *Annu. Rev. Mater. Sci.*, vol. 28, pp. 271-298, 1998
5. Y.I. Denisov-Nikolski, S.P. Mironov and N.P. Omeljanenko, *Actual problems of theoretical and clinical osteoartrology*, Moscow: Novosti, 2005. [in Rus]

6. B.A. Zhilkin, Y.I. Denisov-Nikolski and A.A. Doktorov, "Structural organization and formation of cortical bone", *Uspekhi sovremennoy biologii* [*Advance in modern biology*] vol. 123, no. 6, pp. 590-598, 2003. [in Rus]
7. A.S. Avrunin, R.M. Tikhilov, I. I. Shubniakov, L.A. Parshin, B.E. Melnikov and D.G. Pliev, "Hierarchy of spiral organization of skeletal structures. Interrelationship between structure and functions", *Morfologiia [Morphology]*, vol. 137, no.2, pp. 69-75, 2010. [in Rus]
8. A.S. Avrunin, R.M. Tikhilov, A.B. Abolin and I.G. Shcherback, "Levels of bone mineral matrix organization and the mechanisms determining parameters of its formation", *Morfologiia [Morphology]*, vol. 127, no. 2, pp. 78-82, 2005. [in Rus]
9. M. Buehler, "Molecular nanomechanics of nascent bone: fibrillar toughening by mineralization", *Nanotechnology*, vol. 18, pp. 295102-295110, 2007.
10. B. Yucesoy, L.E. Charles, B. Baker and C.M. Burchfie, "Occupational and genetic risk factors for osteoarthritis: A review", *Work*, vol. 50, no. 2, pp. 261–273, 2015.
11. X.O. Brykalova, N.N. Kornilov, A.A. Cherny, Y.A. Rykov and A.A. Pavlychev, "Electronic and atomic structure of subchondral femoral bone in intact and osteoarthritic knee compartments", *Eur. Phys. J. D.*, vol. 73, 113, 2019.
12. A.A. Pavlychev, A.S. Avrunin, A.S. Vinogradov, E.O. Filatova, A.A. Doctorov, Y.S. Krivosenko, D.O. Samoilenko, G.I. Svirskiy, A.S. Konashuk and D.A. Rostov, "Local electronic structure and nanolevel hirarchical organization of bone tissue: theory and NEXAFS study", *Nanotechnology*, vol. 27, 504002, 2016.
13. V. Heine, "The pseudopotential concept", *Solid State Physics. Advance in Research and Applications*, vol. 24, pp. 1-36, 1970
14. A.S. Konashuk, D.O. Samoilenko, A.Y. Klyushin, G.I. Svirskiy, S.S. Sakhonenko, X.O. Brykalova, M.A. Kuz'mina, E.O. Filatova, A.S. Vinogradov and A.A. Pavlychev, "Thermal changes in young and mature bone nanostructure probed with Ca 2p excitations", *Biomed. Phys. Eng. Express*, vol. 4, 035031, 2018.
15. X.O. Brykalova, N.N. Kornilov, A.A. Pavlychev, "Ca 2p Photoelectron Spectroscopy of Cortical and Subchondral Femoral Bone Tissue in Intact and Damaged Areas", Conference paper SMS 2019, Lisbon, October, 23 - 25. 2019
16. Zhaoxu Tu, Katharina Achazi, Andrea Schulz, Rolf Mülhaupt, Steffen Thierbach, Eckart Rühl. Mohsen Adeli, Rainer Haag, Combination of Surface Charge and Size Controls the Cellular Uptake of Functionalized Graphene Sheets, *Adv. Funct. Mater.* 2017, 27, 1701837

Proceedings of the Joint SMS / NanoMed / EGF 2019 International Conference
Lisbon, Portugal – October 23 – 25, 2019
DOI: https://doi.org/10.26799/cp-sms-nanomed-egf2019

DNA Tetraplex-based Biosensors for Cell Analysis

Anna Dembska[1], Angelika Świtalska[1], Agnieszka Fedoruk-Wyszomirska[2], Bernard Juskowiak[1]

[1]Faculty of Chemistry, Adam Mickiewicz University, Uniwersytetu Poznanskiego 8, 61-614 Poznan, Poland, aniojka@amu.edu.pl, switalskaang@gmail.com, juskowia@amu.edu.pl
[2]Institute of Bioorganic Chemistry, Polish Academy of Science Noskowskiego 12/14, 60-704 Poznan, Poland, agaw@ibch.poznan.pl

Abstract

Among many different types of biosensors for cell analysis there is growing interest in functional nucleic acids. In our research, we focus on developing DNA tetraplex-based probes generating a fluorescent signal in response to changes in environmental conditions (the presence of biometals or pH changes). The different strategies can be used to give analytical signal upon metal- or proton-binding event by G-quadruplexes or i-motifs, respectively. In this communicate, we briefly report our current developments related to applications of fluorescent DNA tetraplexes for cellular measurements.

Keywords: i-motif, G-quadruplex, FRET, fluorescent cytosine analogue, silver nanoclusters (Ag NCs), potassium sensing, intracellular pH, fluorescence imaging

1. Introduction

Functional nucleic acid-based biosensors are emerging tools that are capable of monitoring ions and metabolites in cell populations or whole animals [1]. DNA tetraplexes belong to functional nucleic acids family as they can exhibit either ligand/ion binding or enzymatic activity. GC-rich nucleic acids are able to form two kinds of tetraplexes: G-quadruplexes or i-motifs. Such kind of sequences are often located in gene promoters and telomeres [2].The guanosine-rich (G-rich) strand may adopt a G-quadruplex conformation involving G-quartets [3,4]; whereas the cytosine-rich (C-rich) strand may fold into an i-motif based on intercalated C·C+ base pairs [5,6]. In both cases, we distinguish between intermolecular (composed of 2 or 4 oligonucleotides) and intramolecular tetraplexes. It is also known that a G-quadruplex possesses a channel at its center with a diameter that correlates well with the ionic radius of K^+ (1.3 Å) and Na^+ (1.16 Å); hence, physiological buffer conditions favor their formation [7]. As we mentioned, i-motif is a closely packed tetraplex DNA structure based on C·C+ intercalated base pairs and its formation requires the specific protonation of cytosines at N(3). The properties of G- quadruplexes and i-motifs contributed to employing them for sensor applications as probes generating a fluorescent signal in response to changes in environmental conditions (the presence of biometals or pH changes, respectively). Especially, G- quadruplex analogues have been widely used as molecular tools for detection of potassium ion (K^+) [8], whereas i-motif based nanoswitches and biosensors are suitable for monitoring pH fluctuations in the physiological range [9]. What is important, the different strategies can be used to obtain fluorescence signal upon metal- or proton-binding event, such as incorporating fluorescent nucleobases, excimer or FRET labelling, finally introducing the new fluorescent nanomaterials (e.g. quantum dots (QDs), silver nanoclusters (Ag NCs)) [10].

In this paper, we briefly report our current developments related to applications of fluorescent oligonucleotide probes, based on i-motif or G-quadruplex forming sequences for cellular measurements.

2. Experimental

The oligodeoxyribonucleotides, Ch(F-TBA-T) and ChONC12 were synthesized by Eurogentec (Liège, Belgium) and tC-MB- 520 probe was synthesized by IBA (Germany), (Table 1). All oligonucleootides were purified by reversed phase HPLC and their identities were confirmed by MALDI-TOF MS. All other reagents were purchased from Sigma Aldrich (St. Louis, MO, USA) and were used as received. Milli-Q ultrapure water was used in all experiments.

Table 1: The studied oligodeoxyribonucleotide probes.

Name	Length	Sequence	Company
Ch(F-TBA-T)	23-mer	5'-Ch-(dT FAM)-TTT AGG TTG GTG TGG TTG GAT TT-TAMRA-3′	Eurogentec
ChONC12	15-mer	5'-Ch-CCCACCCACCCACCC-3'	Eurogentec
tC-MB-520	37-mer	5'-Atto520 GTG ATC TAA CCtC CGC CCC GCC CCG CCC CTA CGA TCA C-3'	IBA

2.1. Recording fluorescence spectra of tC-MB-520

Steady-state fluorescence measurements were carried out on a Cary Eclipse spectrofluorometer (Agilent Technologies, Australia) using 0.4×1 cm quartz cuvettes, containing 1 mL of 250 nM probe solution, prefolded in 10 mM cacodylic buffer, pH 7.50. Fluorescence emission spectra were collected from 420 to 700 nm with excitation set at 395 nm (slits 10/10) and from 515 to 700 nm with excitation set at 500 nm (slits 5/5). The fluorescence spectra were recorded after addition of 1M HCl (1 □L). Mean of fluorescence signal at 550 nm from three independent experiments and their SD were plotted for each pH value. All emission spectra were uncorrected.

2.2. Cell culturing

HeLa cells were seeded at a density of 1.2×10^5 cells per well in 4-chamber glass-bottom cell culture dishes (Grenier Bio-One, Kremsmünster, Austria) and cultured in RPMI 1640 antibiotic-free medium (Sigma, Kawasaki, Japan) supplemented with 10% (v/v) fetal bovine serum (FBS) (Gibco), and 1% RPMI 1640 vitamin solution (Sigma, Kawasaki, Japan) at 37 °C under a 5% CO_2 atmosphere. After one day, the cells reached the appropriate density (80–90% confluence) and were placed in fresh RPMI 1640 medium without supplements. Then the tC-MB-520 probe was transfected at 250 nM concentration using Lipofectamine 2000 (1 µl per well) overnight. The visualizations were done after 24 h of treatment. The three other sample sets with Ch(F-TBA-T) (50 nM) were prepared 3.5 h, 2.0 h and 30 min before visualization. The negative control was untreated cells. Before fluorescence confocal microscopy analysis, cells were washed twice with phosphate buffered saline (PBS) and placed in FluoroBright Live Cell Fluorescence Imaging Medium.

2.3. Fluorescence Imaging Experiments

Images were taken with a confocal laser fluorescence inverted microscope using a Spectral Confocal Microscopy TCS SP5 II Leica system equipped with a white light laser (470–670 nm) and a 405 laser, and an environmental cell culture chamber that provided controlled conditions of temperature, CO_2 saturation and humidity. Sequentially scanned live-cell images were collected using a Plan Apo 63 × 1.4 NA oil-immersion objective. Leica LAS AF SP software was used for control of image processing and fluorescence analysis.
The fluorescence imaging was taken using excitation/emission (ex/em) wavelengths as follows:
(a) Atto520 channel, ex/em range = 514/520–640 nm.
(b) tC/Atto520 channel, ex/em range = 405/520–640 nm.
(c) FAM (fluorescein) channel, ex/em range = 480/510–540 nm.
(d) TAMRA channel, ex/em range = 560/595–630 nm.
(e) FRET channel, , ex/em range = 480/595–630 nm.

2.4. Cell lysate preparation

HeLa cells were cultured in RPMI-1640 medium (Sigma) supplemented with 10% fetal bovine serum (FBS, Biowest), 1x RPMI-1640 vitamin solution (Sigma) and 1x antibiotic antimycotic (Sigma) in 5% CO_2 for 48 h. In the next step, cells were trypsinized and subsequently washed 3-times with 1mL PBS to remove any remaining trypsin. Cell extract was prepared from $1.9x10^7$ cells by sonication (3x 15s with 1 min. intervals) in 1 mL deionized water with subsequent centrifugation at 20 000 x g, 5 min. Before spectral measurements, cell extract (1 mL) was centrifuge at 12 000 rpm for 5 min at 5 °C and the supernatant was transfered to a new tube. The centrifugation of the supernatant was repeated 3 times. Finally, the supernatant was diluted to 1% (v/v) in milipore water.

2.5. Synthesis of DNA-Ag NCs and spectral characterization

$AgNO_3$ solution (10 mM, 2.4 µL) was added to DNA solution (3 µM, 1000 µL) prepared in diluted cell lysate (1%, v/v) to provide an Ag^+-to-DNA molar ratio of 12:1 [11]. After incubation for 15 min, this mixture was reduced by adding freshly prepared $NaBH_4$ (10 mM, 2.4 µL) with vigorous shaking. The mixture was then reacted at 4 °C for

DOI: https://doi.org/10.26799/cp-sms-nanomed-egf2019

3 h. The fluorescence spectra of the as-prepared DNA-Ag NCs were recorded using a Jasco FP-8200 spectrofluorometer (Jasco, Japan), and absorption spectra using a Jasco V-750 spectrophotometer (Jasco, Japan).

3. Fluorescent oligonucleotides probes for cellular measurements

3.1. Bioimaging applications of molecular beacons with i-motif in the loop

Molecular beacons are fluorescently labeled single-stranded oligonucleotides with a stem-loop conformation containing a single-stranded loop region that is antisense to the target sequence to be detected [12]. The way to obtain pH-sensitive molecular beacon (MB) is to enclose sequence rich in cytosines into the loop of MB [13,14]. The cytosine-rich sequences are able to form a tetrameric DNA structure with hemiprotonated C–C^+ base pairs, called the i-motif [5,6,10]. Thus, the cytosine-rich loop of MB folds into i-motif upon changes in [H^+], whereas the different strategies can be used to give analytical signal upon proton-binding event. In our previous studies upon the dual-pyrene labeled molecular beacons (MBs) with i-motif in the loop, we found that such MBs can be successfully transfected into living cells, where they accumulate in the lysosomes and are able to react effectively to pH changes induced by chloroquine [13,14].
Recently, we have developed tC-MB-520 probe based on molecular beacon with i-motif in the loop, labeled with the 1,3-diazo-2-oxo-phenothiazine (cytosine fluorescent analogue tC) and Atto520 dye at 5' termini (Table 1). The spectral characterization of fluorescent probe (called tC-MB-520) was performed in the various pH solution and by using UV-vis, CD and steady-state fluorescence spectra measurements. The ability of tC-MB-520 to monitor pH changes was shown in Figure 1.

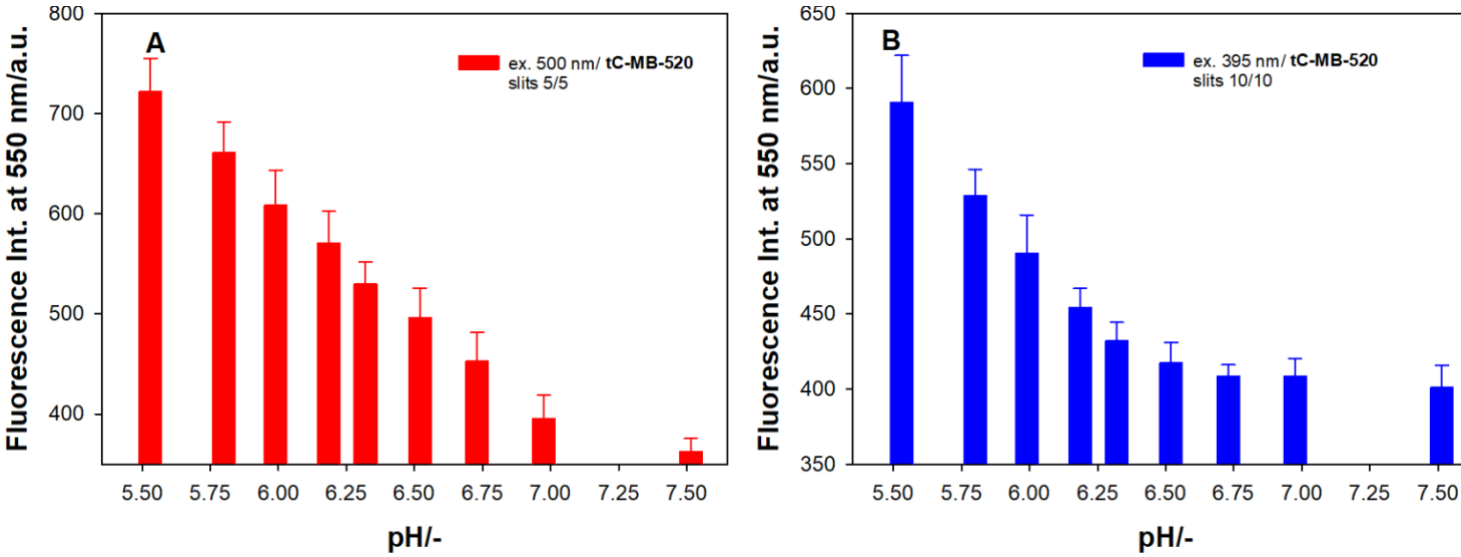

Figure 1. The dependence of fluorescence intensity of tC-MB-520 upon pH changes caused by addition of 1M HCl (1 □L). The excitation wavelength was set at 500 nm (A) or 395 nm (B). Before measurements, 250 nM tC-MB-520 probe was prefolded in 10mM cacodylic buffer, pH 7.50.

Next, we decided to test ability of tC-MB-520 probe to sense pH change in living cells. In our preliminary studies, tC- MB-520 probe was transfected into HeLa cells and the confocal fluorescence imaging of HeLa cells was performed. As shown in Figure 2, it can be clearly observed that the fluorescence signal of Atto520 is distributed as the dots collected in specific organelles, probably lysosomes. The obtained control images indicated that the dot-shaped fluorescence signal was observed only in the HeLa cells treated with tC-MB-520. The further experiments verifying usefulness of tC-MB-520 probe for the quantitative pH analysis *in cellulo* are planned.

DOI: https://doi.org/10.26799/cp-sms-nanomed-egf2019

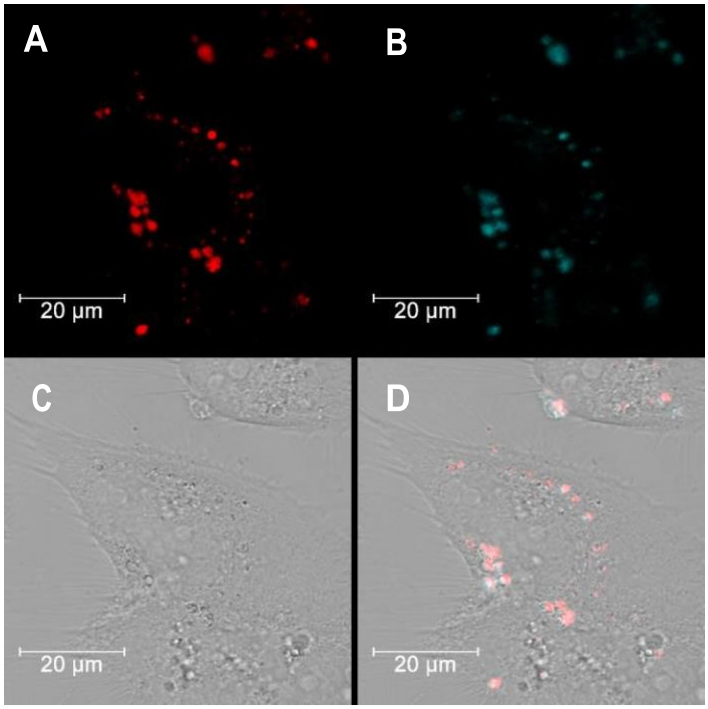

Figure 2. Confocal microscopy images of HeLa cells transfected with 50 nM tC-MB-520 using Lipofectamin 2000: (A) Atto520 fluorescence, marked red; (B) tC/Atto520 fluorescence, marked blue (C) white image (D) overlay of all images. Fluorescence emission filters: 1) for red color, 520-640 nm; excitation wavelength: 514 nm; 2) for blue color, 520-640 nm; excitation wavelength: 405 nm. Scale bars: 20 µm.

3.2. G-quadruplex interaction with cell membrane

In our group, we developed cholesterol-anchored fluorescent probes based on G-quadruplexes for spontaneous anchoring into the hydrophobic interior of living cell membrane [15]. The Ch(F-TBA-T) probe was labeled with carboxyfluorescein (FAM) and carboxytetramethylrhodamine (TAMRA) dyes (Table 1) and showed a very high binding preference for K^+ over Na^+ ions. Precisley speaking, the Ch(F-TBA-T) probe showed a dynamic range for K^+ detection of 2–10 mM in the presence of 150 mM Na^+, which is a clinically important concentration range of K^+ under an extracellular conditions. Fluorescent bioimages indicated the sponatneous anchoring of the Ch(F-TBA-T) to the outer cell membrane of HeLa cells within 0.5 h after adding probe into medium. The longer contact of Hela cells with Ch(F-TBA-T) probe (> 2 h) resulted in diffusion of the probe into nucleus of the cells (Figure 3). What is important, the analogous probe without cholesterol moiety was not only unable to anchor to the cell membrane, but also did not penetrate inside the cells [15].

DOI: https://doi.org/10.26799/cp-sms-nanomed-egf2019

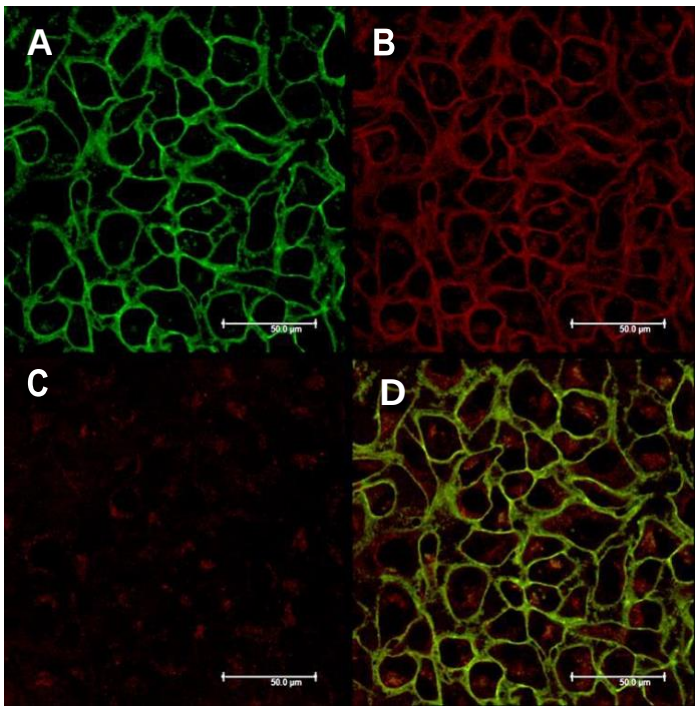

Figure 3. Confocal microscopy images of HeLa cells treated with 50 nM Ch(F-TBA-T) for 3.5 h: (A) FAM fluorescence, marked green; (B) FRET image, marked red; (C) TAMRA image, marked red; (D) overlay of all images. Fluorescence emission filters: 1) for FAM, 510-540 nm; excitation wavelength: 480 nm; 2) for FRET, 595-630 nm; excitation wavelength: 480 nm; 3) for TAMRA, 595- 630 nm; excitation wavelength: 560 nm. Scale bars: 50 μm.

3.3. DNA-Ag NCs synthesized in cell lysate

In recent years, a huge progress has been made regarding the development of new fluorescent nanomaterials such as quantum dots (QDs) or silver nanoclusters (Ag NCs), which are an alternative to organic fluorophores, due to high quantum efficiency, photostability, ability to manipulate their emission spectrum or large Stokes shifts. Therefore, we have started to develop probes based on silver nanoclusters. Ag^+ is uniquely interesting because it exhibits unusually specific interactions with DNA, binding exclusively to natural bases rather than the negatively charged phosphate backbone [16]. The potential that Ag^+-DNA interactions hold for nanotechnology is already exemplified by the fluorescent, DNA-stabilized silver clusters used recently in novel chemical and biochemical sensing schemes [17]. These nano-optical, DNA based materials are known to incorporate Ag^+ as well as neutral silver atoms, indicating that Ag^+-DNA interactions are key to stabilizing the fluorescent clusters [18]. The goal of our work is to utilize DNA rich in cytosine base (ChONC12) equipped with a cholesterol anchor (Table 1) as a scaffold for the synthesis of silver nanoclusters.

We synthesized the ChONC12-Ag NCs nanoclusters by adding sodium borohydride to a cell lysate solution of silver nitrate and the ChONC12 oligonucleotide under air, as described in the literature [19]. The formation of the nanoclusters during the reduction step was evident from the appearance of a yellow color.

Several electronic transitions are also observed in the absorption spectra of the ChONC12/Ag NCs conjugates (Figure 4A). A primary distinguishing feature of the nanoclusters is their strong peak at 440 nm that is red-shifted and narrower relative to the plasmon transition of the nanoparticles. In addition, bands at 350, 500, and 650 nm are observed for the ChONC12-Ag NCs nanoclusters. These bands are all considered indicative of genuine nanoclusters because they are absent from the absorption spectrum of silver nanoparticles, which only displays one broad peak at λmax= 405 nm [19].

DOI: https://doi.org/10.26799/cp-sms-nanomed-egf2019

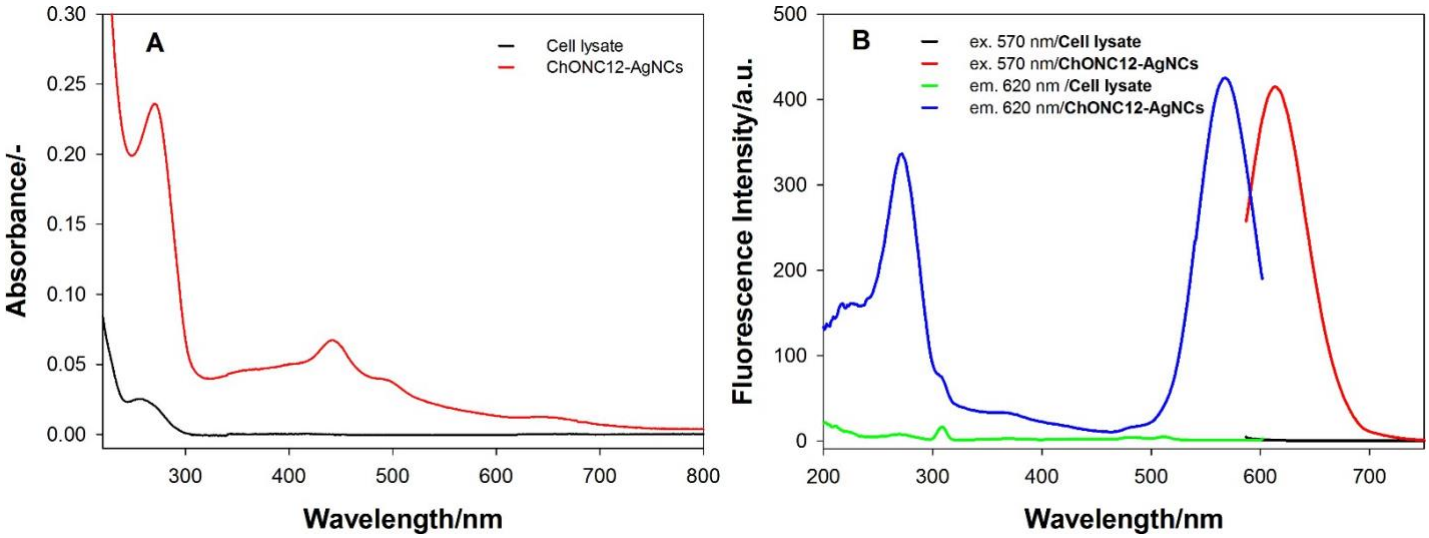

Figure 4. Absorption spectra (A) and fluorescence spectra (B) of the ChONC12-Ag NCs. The solutions contained 2 µM ChONC12- DNA, cell lysate diluted in water (1% v/v), $[Ag^+]=[BH^-]=24$ µM, λ_{ex} =560 nm.

The sequences and lengths of the DNA strands play significant roles in determining the sizes of the DNA-Ag NCs and, thus, their optical properties; in contrast, the Ag^+/DNA molar ratio determines the fluorescence intensity [11,20,21]. The as- prepared ChONC12-Ag NCs fluoresced at 620 nm when excited at 570 nm (red line, Figure 4B). These transitions are in the spectral region for small silver nanoclusters, as expected from theoretical and experimental studies [22-24]. One attractive feature of the ChONC12-Ag NCs is that they fluoresce only in the near-IR region, thereby providing optical transparency and lower background fluorescence when analyzing biological tissues.

4. Conclusions

We have demonstrated that molecular beacon, tC-MB-520 integrated with the i-motif, labeled with fluorescent cytosine analogue (tC) and Atto520 dye at 5' termini, can be used to monitor pH changes in the range from 5.5 pH to 7.0. Moreover, tC-MB-520 probe could be successfully transfected into living cells.
The structurally simple cholesterol-based fluorescent G-quadruplexes have good potential for *in vivo* monitoring the transport of K^+ ions through the sodium-potassium pump. We also tested DNA rich in cytosine base (ChONC12) equipped with a cholesterol anchor as a scaffold for the synthesis of silver nanoclusters in HeLa cell lysate. Have obtained the highly fluorescence nanoclusters, we are planning to integrate ChONC12/Ag NCs and G-quadruplex DNA. However, additional work is needed to understand the properties of DNA-templated Ag NCs in cellular conditions, where they may be used for imaging applications.

Funding

This research was financed by the National Science Centre of Poland, Grant No. 2015/19/N/ST4/00407 and Grant No.
2015/17/B/ST4/03627.

Acknowledgements

Experiments using confocal microscopy were performed in the Laboratory of Subcellular Structures Analyzes at the Institute of Bioorganic Chemistry of the Polish Academy of Sciences, Poznan, Poland. Authors thank Daria Orligóra for technical support.

References

1. A. Alsaafin and M. McKeague, "Functional nucleic acids as in vivo metabolite and ion biosensors," *Biosensors and Bioelectronics*, vol. 94, pp. 94-106, 2017.T.A. Brooks, S. Kendrick, L. Hurley, "Making sense of G-quadruplex and i-motif functions in oncogene promoter," *FEBS J.*, vol. 277, no. 17, pp. 3459-3469, 2010.
2. D. Sen and W. Gilbert "Formation of parallel four-stranded complexes by guanine-rich motifs in DNA and its applications for meiosis", *Nature*, vol. 334, pp. 364–366, 1998.
3. W.I. Sundquist and A. Klug, "Telomeric DNA dimerizes by formation of guanine tetrads between hairpin loops," *Nature*, vol. 342, 825–829, 1989.

4. K. Gehring, J.-L. Leroy, M. Guéron ”A tetrameric DNA structure with protonated cytosine-cytosine base pairs,” *Nature*, vol. 363, pp. 561–565, 1993.
5. J.-L. Leroy, M. Guéron, J.L. Mergny, C. Hélène, ”Intramolecular folding of a fragment of the cytosine-rich strand of telomeric DNA into an i-motif,” *Nucleic Acids Res.*, vol. 22, pp. 1600–1606, 1994.
6. D.M. Kong, Y.E. M,a J.H. Guo, W. Yang, H.X. Shen, ”Fluorescent sensor for monitoring structural changes of G- quadruplexes and detection of potassium ion,” *Anal. Chem.*, vol. 81, pp. 2678–2684, 2009.
7. S. Takenaka, B. Juskowiak, ”Fluorescence Detection of Potassium Ion Using the G-Quadruplex Structure, ” *Anal. Sci*., vol. 27, pp. 1167 -1172, 2011.
8. A. Dembska, ”The analytical and biomedical potential of cytosine-rich oligonucleotides: A review,” *Anal. Chim. Acta*, vol. 930, pp. 1-12, 2016.
9. A. Dembska, P. Bielecka, B. Juksowiak, ”pH-Sensing fluorescence oligonucleotide probes based on an i-motif scaffold: a review,” *Anal. Methods*, vol. 9, pp. 6092-6106, 2017.
10. G.-Y. Lan, C.-C. Huang, H.-T Chang, ”Silver nanoclusters as fluorescent probes for selective and sensitive detection of copper ions,” *Chem. Commun.*, vol. 46, no. 8, pp.1257-1259, 2010.
11. S. Tyagi and F.R. Kramer, ”Molecular beacons: probes that fluoresce upon hybridization,” *Nat. Biotech.*, vol. 14, pp. 303-308, 1996.
12. A. Dembska, B. Juskowiak, ”Pyrene functionalized molecular beacon with pH-sensitive i-motif in a loop,” S*pectrochim. Acta A*, vol. 150, pp.928-933, 2015.
13. A. Dembska, E. Kierzek, B. Juskowiak, ”Studying the influence of stem composition in pH-sensitive molecular beacons onto their sensing properties,” *Anal. Chim. Acta*, vol. 990, pp. 157-167, 2017.
14. A. Switalska, A. Dembska, A. Fedoruk-Wyszomirska, B. Juskowiak, ”Cholesterol-Bearing Fluorescent G-Quadruplex Potassium Probes for Anchoring at the Langmuir Monolayer and Cell Membrane,” *Sensors*, vol. 18, 2021, 2018.
15. L. Berti and G.A. Burley, ”Nucleic acid and nucleotide-mediated synthesis of inorganic nanoparticles,” *Nat. Nanotechnol.*, vol. 3, pp. 81–87, 2008.
16. Z. Yuan, Y.-C. Chen, H.-W. Li, H.-T. Chang, ”Fluorescent silver nanoclusters stabilized by DNA scaffolds,” *Chem. Commun.* 2014. doi:10.1039/c4cc02981j.
17. D. Schultz, K. Gardner, S.S. Oemrawsingh, N. Markešević, K. Olsson, M. Debord, D. Bouwmeester, E. Gwinn, ”Evidence for rod-shaped DNA-stabilized silver nanocluster emitters,” *Adv. Mater.*, vol. 25, pp. 2797–2803, 2013.
18. C.M. Ritchie, K.R. Johnsen, J.R. Kiser, Y. Antoku, R.M. Dickson, J.T. Petty,”Ag Nanocluster Formation Using a Cytosine Oligonucleotide Template,” *J. Phys. Chem. C*, vol. 111, pp.175–181, 2007.
19. C.I. Richard, S. Choi, J.-C. Hsiang, Y. Antoku, T. Vosch, A. Bongiorno, Y.-L. Tzeng, R.M. Dickson, ”Oligonucleotide- stabilized Ag nanocluster fluorophore,” *J. Am. Chem. Soc.*, vol. 130, pp. 5038–5039, 2008.
20. H. Deng and H.T. Yu,”A Mini Review on Controlling the Size of Ag Nanoclusters by Changing the Stabilizer to Ag Ratio and by Changing DNA Sequence,” *Adv. in Natural Sci.*, vol. 8, no. 2, pp.1-9, 2015.
21. I. Rabin, W. Schulze, G. Ertl, ”Light emission during the agglomeration of silver clusters in noble gas matrixes,” *J. Chem. Phys.*, vol. 108, no. 12, pp. 5137-5142, 1998.
22. S. Fedrigo, W. Harbich, J. Buttet, ”Optical response of Ag2, Ag3, Au2, and Au3 in argon matrixes” *J. Chem. Phys.*, vol. 99, no. 8, pp. 5712-5717, 1993.
23. V. Bonacic-Koutecky, J. Pittner, M. Boiron, P. Fantucci, ”An accurate relativistic effective core potential for excited states of Ag atom: An application for studying the absorption spectra of Agn and Agn(+) clusters” *J. Chem. Phys.*, vol. 110, no. 8, pp. 3876-3886, 1999.

Proceedings of the Joint SMS / NanoMed / EGF 2019 International Conference
Lisbon, Portugal – October 23 – 25, 2019
DOI: https://doi.org/10.26799/cp-sms-nanomed-egf2019

Concept and economic evaluation of an automotive composite part with integrated wireless sensorsystem

M. Hardt [1,*], Prof. P. Middendorf [2], Prof. R. Bjekovic[3]
[1] Daimler AG, Stuttgart, Germany
[2] Institut of Aircraft Design, University of Stuttgart,
[3] University of Applied Science Ravensburg-Weingarten

Abstract:

In addition to traditional research and development topics, such as lightweight construction, the automotive industry is currently facing a variety of challenges in the areas of connectivity, autonomous driving, mobility services and electrification. These development directions will be further intensified in the future, leading to a significant increase in electronic and sensor components in vehicles [1]. Continuing miniaturization of components on the one hand and reduction of costs on the other hand enable completely new possibilities for integrated functionalities.
One research approach that takes into account both the requirements for consistent lightweight construction and for integrated functionalities is sensor-integration in fiber composite materials. Due to their high lightweight potential as well as the specific manufacturing process using different plies of materials, fibre reinforced plastics (FRPs) or composites are the ideal material for sensor-integrated components [2], [3].
In the context of this work, the integration of a wireless sensor system into an automotive series component made of carbon fiber reinforced plastic (CFRP) is presented. It is shown how a component platform with a multifunctional range can be manufactured from a conventional structural component (Fig. 1). The design and integration of the sensor system is based on the specific requirements of the Resin-Transfer-Moulding (RTM) process as an established manufacturing process for CFRP components as well as specific functional requirements of a sensor-integrated component in automotive engineering.
The integration of sensor systems into CFRP enables a multitude of new functions, which in turn can have a positive effect on the cost-benefit ratio of the product. Process monitoring for quality improvement during production or predictive maintenance of the composite part but also of the surrounding parts and components in the usage phase are obvious use-case examples. Based on the integrated sensor system, the manufacturing process and the potential applications the requirements for a cost estimation model are specified.

Keywords: automotive composites, functional integration, sensorintegration, wireless sensorsystem, resin-transfer-moulding, process-monitoring, costestimation

Figure 1: Technology Demonstrator - sensor-integrated CFRP spare wheel recess [4]

Introduction:

DOI: https://doi.org/10.26799/cp-sms-nanomed-egf2019

Starting from four projects, funded by the BMBF (German Federal Ministry of Education and Research), researchers from science and industry are working together in the ARENA2036 research campus (Active Research Environment for the Next Generation of Automobiles in 2036) on the core topics of work, mobility and production of the future. The research topics of ARENA2036 are oriented along the entire value chain of product development - from the project idea and conceptual design to digital processing and production. One of the four core projects is the Project LeiFu (Intelligent Lightweight Construction with Function Integration)
Within the LeiFu project, the research approach of lightweight constructions with integrated functionalities (Fig. 2) is being pursued. Lightweight materials offer ideal conditions and excellent possibilities for integrating mechanical, thermal, sensory and electrical functions into components. The weight reduction of vehicle components can be identified as a major contribution to reduce carbon dioxide emissions from conventional motor vehicles and to increase the range of electric vehicles and is an essential research component of the LeiFu project. Like the other projects of ARENA2036, the project was launched in 2013 with a project duration of five years in order to develop a lightweight underbody structure that meets the high requirements for successful weight reduction. The reduction in the weight is achieved in two ways. On the one hand, the potential of lightweight materials and sandwich structures is being exploited. On the other hand, individual technologies have been developed that are integrated directly into the underbody structure of the vehicle[5].

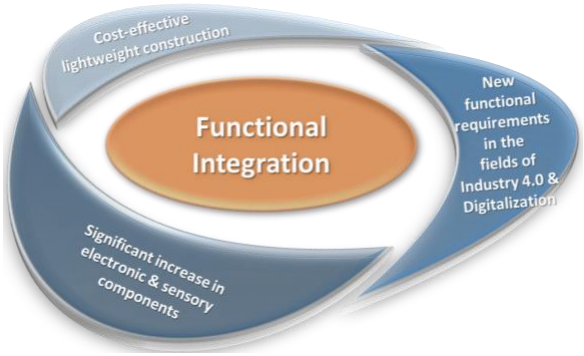

Figure 2: Motivation for functional integration in composites structures

Integration of sensors in automotive engineering and lightweight design of CFRP components:

The application of sensors in automotive engineering is a very important and strongly growing area of importance. Up to 100 sensors are installed in current luxury vehicles, in exceptional cases even up to 150. The sensors are primarily used in the fields of safety, comfort and powertrain.
In addition to these conventional areas of application for automotive sensors, future generations of vehicles will be highly characterized by the use of sensors for driver assistance systems, for monitoring vehicle occupants (e.g. monitoring vital parameters) and for monitoring vehicle parameters (SHM).
Apart from optimizing established sensor principles, these new fields of application increasingly require the development of new sensor concepts and technologies. In addition to high technical requirements, the resulting sensor systems are also subject to ever higher demands in terms of costs, miniaturization, quality and reliability.

Integration of sensors in automotive composite components:

The integration of sensors in composite components is a scientific field that demands a high level of interdisciplinary cooperation. In addition to technical questions from materials science, electrical engineering, information technology and sensor technology, economic questions for use in automobile applications must also be considered.
Currently, sensors in automotive engineering are mainly applied to the corresponding components. On the one hand, this entails additional weight due to the housing and cables. On the other hand, the assembly time is also increased due to the additional process steps.

DOI: https://doi.org/10.26799/cp-sms-nanomed-egf2019

One way of counteracting this problem is to integrate the sensors and further electronic components (Fig. 3), directly into the corresponding component or into the material itself. This is possible due to the constant progress in the miniaturization of sensor systems and by the use of innovative sensor systems such as MEMS (microelectromechanical systems), fiber-based or printed sensors.

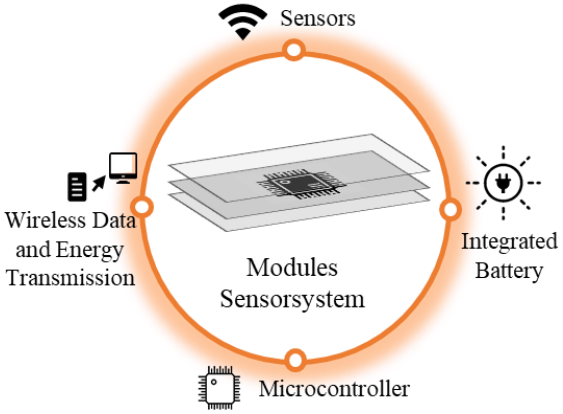

Figure 3: Modules of the integrated sensorsystem [6]

There are already a variety of approaches to integrated sensors that focus on monitoring the condition of machines or components. However, the approach in this project aim of integrating the sensors into the components themselves.

Potential applications of automotive composites with integrated sensorsystems:

In addition to substituting existing solutions and functions, the purpose is also to implement completely new functionalities that are only possible by the integration of sensors. This includes, for example, the complete monitoring of a component from production, logistics and operation in the vehicle to upcoming inspections whose necessity is established by the component itself (Fig. 4).
One of the largest potential fields of application is currently the condition monitoring of fiber composite structures. Due to their specific laminate structure, it is possible to produce components with tailor-made properties through defined positioning and layering of fibers and textiles. This is particularly necessary for applications with the highest lightweight construction requirements, as demand in aerospace and automotive engineering. The variation of the resin system opens up a further level of freedom for the specific modification of component properties. In addition to the high potential for lightweight construction, composites also offers ideal conditions for the integration of sensor systems due to their layered structure and the used manufacturing processes.

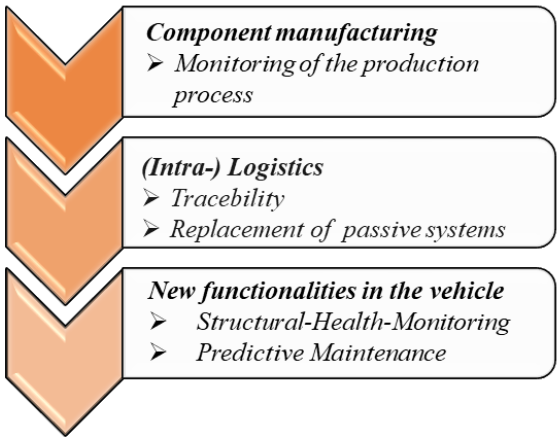

Figure 4: Potential applications and added values

DOI: https://doi.org/10.26799/cp-sms-nanomed-egf2019

Requirements for the cost estimation model:

For the implementation of a new technology in automotive engineering, it is often essential to assess the economic efficiency of this technology.
Currently there are no suitable methods available with which the economic efficiency of sensor-integrated composites can be accurately assessed. Therefore it is necessary to develop a cost estimation model that can be applied in the early phase of research and product development. For this purpose it is important to identify the relevant cost drivers and thereby make them calculable. For the specific application, the following requirements are defined, which should be fulfilled by the cost model:
The manufacturing costs of the sensor-integrated component must be calculated precisely. Further on, potential applications and resulting cost savings of the manufacturing phase have to be considered. On the basis of these calculations it should then be possible to make a prediction on the economic efficiency of the integrated sensor system and thus a recommendation for futher decision making.

The concept of the cost estimation model is shown below (Fig. 5).

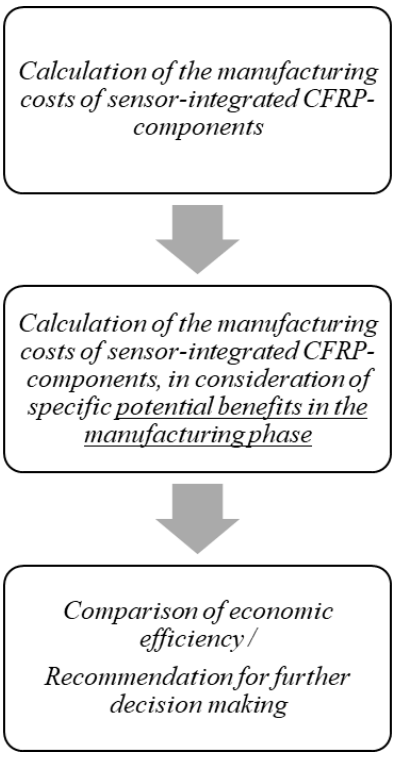

Figure 5: Concept of a cost estimation model for sensor-integrated composites [4]

Conclusions:

A concept for the integration of sensor technology into composite components in automotive applications could be shown on the basis of the technology demonstrator “sensor-integrated CFRP spare wheel recess”. The concept is based on the integration of a complete sensor system consisting of sensors, modules for wireless data and power transmission as well as a microcontroller for data evaluation.
With the additional sensor modules, a wide range of potential benefits can be realized over the entire product life cycle of the sensor-integrated component. The sensor system makes it possible to realize the potential applications of process monitoring, which have already been successfully demonstrated in a number of experiments [7]. Further applications in logistics and in vehicle use (SHM) are also conceivable with the presented concept.
Requirements for a cost-benefit assessment model are defined on the basis of the technical specifications of the sensor system and the identified potential benefits. This concept will be used in the future as a basis for the development of a cost estimation model for sensor-integrated composites.

Acknowledgements:

The present work is linked to the research and development project ARENA2036, funded by the Federal Ministry of Education and Re-search (BMBF) within the framework of the projects *LeiFu (Intelligent Lightweight Design with functional integration)* and *FlexCar (A technology platform concept for future cyberphysical mobility)* coordinated by the Project Management Agency Karlsruhe (PTKA).

References:

1. W. Fleming, "New Automotive Sensors – A Review," IEEE Sensors J., vol.8, no. 11, pp. 1900-1921, Nov. 2008.
2. K. Moghaddam, et al., "Sensor Integration in Fiber-Reinforced Polymers: Technology and Applications", Material-Integrated Intelligent Systems - Technology and Applications, pp. 159-200, 2018, Wiley-VCH.
3. B. Fox, et al., „Smarte Kunststoff-Bauteile für Automotive Innovation und Industrie 4.0", ZWF - Zeitschrift für wirtschatflichen Fabrikbetrieb 112 (7/8), pp 522-525, 2017, Carl Hanser Verlag.
4. Hardt, M.; Middendorf, P.: An approach to evaluating the economic efficiency of CFRP-components with structure-integrated sensor systems., Conference WerkstoffPlus Auto, Stuttgart, 2019.
5. P. Böhler, et al., „ARENA2036 - Der Forschungscampus für Arbeit, Mobilität und Produktion der Zukunft", wt Werkstattstechnik online 108 H. 3, pp. 124-131, 2018, Springer Verlag.
6. Hardt, M., Hoßfeld, M., Ackermann, C. et al. ATZ Prod Worldw (2019) 6: 10. https://doi.org/10.1007/s38312-019-0048-1
7. Damm, A; Ritter, F.; Middendorf, P.: Process and component monitoring though structure-integrated sensors, Conference WerkstoffPlus Auto, Stuttgart, 2019.

Proceedings of the Joint SMS / NanoMed / EGF 2019 International Conference
Lisbon, Portugal – October 23 – 25, 2019
DOI: https://doi.org/10.26799/cp-sms-nanomed-egf2019

Magnetic and Electrical Properties of postannealed Co_2MnSi Heusler alloy films

G. Grigaliūnaitė-Vonsevičienė[1],B. Vengalis[2], A. Maneikis[2] and R. Juškėnas[2]

[1]Vilnius Gediminas Technical University,
Saulėtekio al. 11, LT-10223 Vilnius, Lithuania, grazina.grigaliunaite-vonseviciene@vgtu.lt
[2]Center for Physical Sciences and Technology,
Saulėtekio al. 3, LT-10223 Vilnius, Lithuania, bonifacas.vengalis@ftmc.lt

Abstract

In this work, the Co_2MnSi films (d=90-120 nm) were grown by dc magnetron sputtering of a stoichiometric target on MgO(100) and Si(100) followed by annealing in vacuum at $T=T_a$=200□500□C. Formation of nanocrystalline structure with typical grain size 20□40 nm has been indicated from SEM surface images for the films grown either on Si or MgO. XRD investigations revealed amorphous state for the as prepared films while partially ordered B2 structure and traces of highly ordered L21 structure have been indicated for the films annealed at T_{ann}>300□C.The alternating current (AC) magnetic susceptibility (□□dM/dH) was investigated at RT and 78 K to reveal evolution of magnetic properties of the prepared films with annealing. Increase of saturation magnetisation and reduced electrical resistance have been indicated with T_a increasing from 300 to 400□C. Meanwhile, long term annealing of the films at T_{ann}□ 450□C resulted reduced saturation magnetization values.

Keywords: Heusler thin films,Co_2MnSi, annealing, magnetic and electrical properties

1. Introduction

The Co_2MnSi (CMS) Heusler alloy is known as a strong ferromagnet with high Curie temperature (T_C□985 K), large minority-spin band gap of 0.4 eV and saturation magnetization Ms of about 5.1 □B/f.u. at 4 K. The material provides increasing scientific and technological interest due mainly to full spin polarization of carriers and thus it is promising for the fabrication of magnetic tunneling junctions, spin filters, and other spintronics devices operating at room temperature [1].
Both the saturation magnetization and residual resistivity of the compound were found to depend on structural and spin disorder [2, 3]. Magnetic and electrical properties of the CMS films are known to depend on crystalline structure and chemical ordering of the constituent elements.
The CMS compound exists in three different structural variants. The L21 ordered structure with a cubic unit cell composed of four interpenetrating fcc lattices, each occupied solely by Co, Mn or Si atoms, the B2 structure with the Mn and Si atoms randomly occupying the Mn and Si sublattices and the A2 structure with all four sublattices occupied at random by Co, Mn and Si atoms, corresponding to a simple bcc lattice with random site occupancy [4].
Unfortunately, evolution of electrical and magnetic properties of Heusler alloys has not been fully understood yet, although efforts have been undertaken to investigate complex physics of the CMS films prepared by using various deposition techniques (molecular beam epitaxy, magnetron sputtering, laser ablation, plasma- assisted sputtering) on different substrates (Ge, Si, Al2O3, MgO, GaAs and others)..
In this paper, we report the research results on the CMS films (d=90-120 nm) grown by dc magnetron sputtering of a stoichiometric target on MgO(100) and Si(100) substrates followed by annealing in vacuum at T_{ann}=200□500□C. Influence of post-annealing on magnetic and electrical properties have been investigated. Magnetic properties of CMS films prepared under various deposition or post annealing conditions were explored by applying alternating current (AC) magnetic susceptibility method [5].

2. Preparation and experimental

The CMS films were prepared by DC magnetron sputtering method in high vacuum chamber with residual gas pressure □3 10^{-5} Pa onto commercially available Si(001) substrates and MgO single crystals with cleaved (001) faces. The Si and MgO substrates were cleaned by washing them in acetone in ultrasonic bath for 15 minutes following by rinsing in distilled water and drying in nitrogen flow. $Co_{0.50}Mn_{0.25}Si_{0.25}$ films were grown at room temperature using pre-sputtered CMS target at constant growth rate ~4.0 nm/min. The Ar gas pressure during

DOI: https://doi.org/10.26799/cp-sms-nanomed-egf2019

sputtering was of about 3 Pa for all the prepared films. Thickness of the CMS films (d = 90□110 nm) was controlled by deposition duration. After deposition, the CMS thin films were *in-situ* annealed in vacuum at various temperatures ranging from RT to 500□C. The films were cooled down to RT in the vacuum.
Thickness of few selected CMS samples was measured precisely by the DECTAC 6M profilometer. The structural properties of Heusler alloys were analyzed by X-ray diffraction patterns in the □-2□ geometry using X-ray diffractometer with $CuK_{\alpha 1}$ radiation source.
Proof of the $L2_1$ phase is related to the characteristic (220) XRD diffraction reflex. The X-ray diffraction patterns in the □-2□ geometry were measured for 110 nm thick CMS film grown on Si (001) and annealed subsequently in vacuum 1h at 500^0 C. SEM surface images revealed presence of grains in the annealed films with the average diameter of about 15nm.
Magnetic properties of the CMS films were explored by applying alternating current (AC) magnetic susceptibility method [5]. The coil assembly (see Fig. 1), used in this work consisted of magnetically coupled (1) primary coil (600 turns) and (2) secondary coil (2 sections, 300 turns each). The secondary coil consisted of two halves wounded in opposite sense to make the total induced voltage equal to zero. The off-balance signal observed in the absence of the sample has been avoided from the measured signal numerically. The method is based on the measurement of response of magnetization (dM/dH) induced by an oscillating magnetic field in a limit of small AC magnetic field, H_{AC}. $H_{AC}<10^2$A/m. The output AC voltage, $V_{AC,}$ was induced when sample was moved into one of two sections due to a time-dependent magnetisation of the sample resulting change of mutual inductance. AC in primary coil was kept fixed □1mA. The applied DC field H was changed in the limits from -300 to 300 kA/m. The applied field was directed parallel to the coil axis, i. e., parallel (antiparallel) to the AC field. The detected signal was measured in a narrow frequency band in the vicinity of .

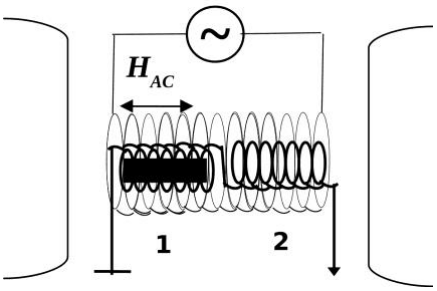

Fig. 1: Experimental scheme of coils used for AC susceptometer.

3. Results and discussion

The alternating current (AC) magnetic susceptibility (□□dM/dH) was investigated at RT and 78 K to reveal evolution of magnetic properties of the prepared films with annealing. Increase of saturation magnetisation and reduced electrical resistance have been indicated with Ta increasing from 200 to 300□C. Negligible changes of □(H) curves have been indicated for the films with long term annealing in air at T □ 200□C (see curve 1 in Fig. 2 measured for the CMS/Si film (d = 250 nm) annealing additionally in air for 3h). However, significant changes of both coercive field (Hc) and satturation magnetisation (M_{sat}) values have been indicated for the films grown either on Si or MgO substrates with their annealing at 300□C.

DOI: https://doi.org/10.26799/cp-sms-nanomed-egf2019

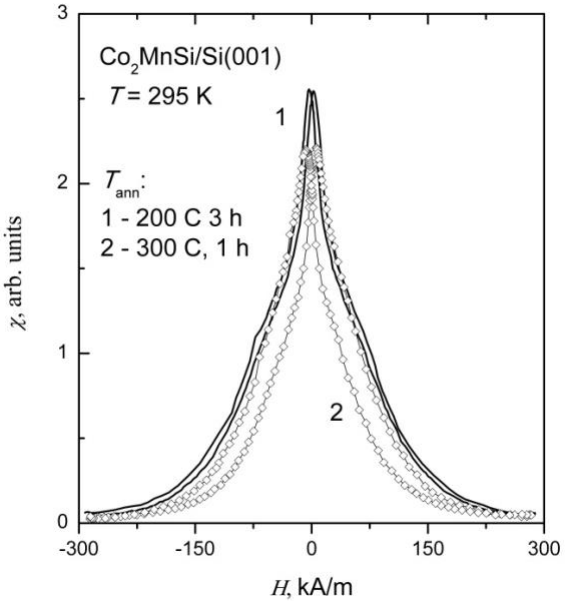

Fig. 2: Magnetic field-dependent AC magnetic susceptibility □□dM/dH and magnetisation, *M*, measured at RT for Co_2MnSi/Si(001) films annealed in vacuum at 200 □C for 3 h (1), 300□C for 1 h (2).

The alternating current (AC) magnetic susceptibility (χ~dM/dH) was investigated at RT to reveal evolution of magnetic properties of the prepared films with annealing. Increase of the saturation magnetisation and reduced electrical resistance have been indicated with T_{ann} increasing from 300 to 400°C. Meanwhile, long term annealing of the films at $T \geq$ 450°C resulted reduced saturation magnetization values (Fig 2).

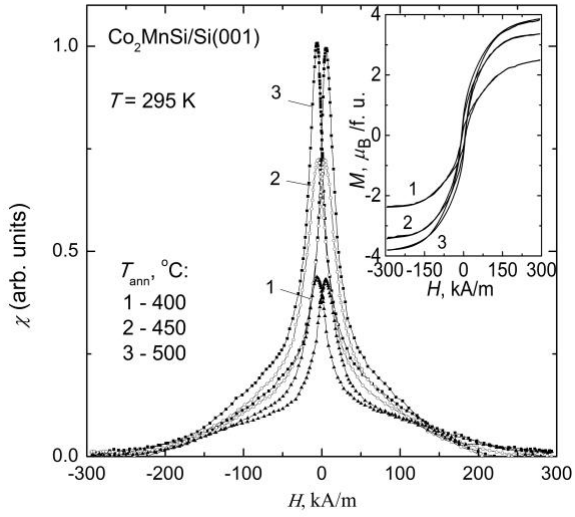

Fig. 3: $\chi(H)$ and $M(H)$ dependencies due to annealing temperature from 400° C to 500° C.

In Fig. 3 we show also significant change in the shape of the characteristic $\chi(H)$ curves with film annealing. The $\chi(H)$ dependences measured after annealing of the films at $T_{ann} \geq$400 °C demonstrated occurrence of a narrow peak in the low field region (with the half width at half maximum of about 40 kA/m). The observed complex shape of the $\chi(H)$ curves may be understood assuming that magnetisation of the films is defined by different (smaller and larger) grains. Thus, we do believe that the observed peak-like $\chi(H)$ behavior in the low field region ($|H| \leq$ 50 kA/m) may be associated to the magnetisation reversal process caused by larger grains exhibiting highly ordered $L2_1$(or partially ordered B2) structure while variation of $\chi(H)$ at higher fields ($|H|$ = 50÷200 kA/m) could be associated either to the magnetisation of smaller grains or amorphous matrix.
Field-dependent magnetisation of the films per formula unit, $M(H)$, shown in Fig. 3 inset has been obtained numerically.

DOI: https://doi.org/10.26799/cp-sms-nanomed-egf2019

The coercive field values estimated for the films from their magnetisation loops (see inset in Fig. 3) correlated well with the corresponding $\chi(H)$ peak positions in Fig. 3. The M_{sat} values were found to increase with T_{ann} with the highest value of about 4.0 μ_B/f. u. (at T =295 K) estimated for the CMS/Si film annealed at 500 °C.
The estimated coercive field values (at room temperature and at 78 K) for CMS films (d~110 nm) grown in-situ on heated Si and MgO substrates and those deposited onto non heated substrates followed by annealing in vacuum at different annealing temperatures (T_a) are summarised in Table 1.

Table 1: The coercive field H_c at room temperature for CMS films (d~110 nm) grown in-situ at different temperatures T_s**,** and onto non heated substrates with following annealing for 1h in vacuum at different temperatures T_a.

Film/substrate	T_s, °C	H_c(295K), kA/m	T_{ann}, °C	H_c(78K), kA/m	H_c(295K), kA/m
CMS/Si(001)	400	0.4	400	9.2	6.0
	450	2.4	450	8.0	5.7
	500	1.6	500	8.4	6.8
CMS/MgO(001)	400	0.1	400	9.32	5.7
	450	0.4	450	8.9	5.7
	500	0.2	500	9.1	6.1

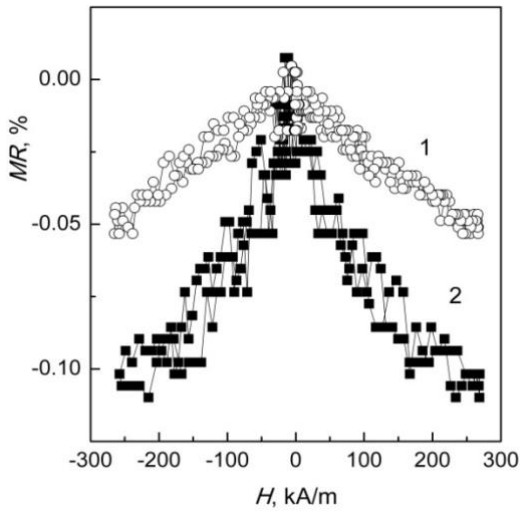

Fig. 3: Magnetic field-dependent magnetoresistance ofthe CMS/Si film annealed preliminary in vacuum at 450 °C followed by additionall annealing in air at 200°C for 3 h (1) and the CMS/MgO film grow in-situ at 500°C (2).

Relatively low values of negative magnertoresistance (MR) shown in Fig. 4 were measured for the CMS/Si film annealed preliminary in vacuum at 450 °C followed by additional annealing in air at 200°C for 3 h (1) and for the CMS/MgO film grow in-situ at 500°C. The *MR* was found to vary linearly with the magnetic field. At low magnetic fields, however, the *MR* changed nonlinearly with the magnetic field and was strongly temperature-dependent. The *MR* was governed by intergrain scattering due to spin-polarized tunneling

4. Summary and Conclusions

We point out 3 major competing processes having great influence on magnetic and electrical properties of the films, namely, nucleation of nanometric grains in the beginning of the annealing, diffusion-controled formation of the ordered B2 and L21 structures and dissociation of highly ordered L21structure with annealing at T 450°C. Instability of the $L2_1$ structure at the highest annealing temperatures we associate to a possible Si phase segregation at grain boundaries of the prepared nanocrystalline CMS films. Correlation between magnetoresistance of the prepared polycrystalline CMS films, *MR*(*H*), and AC magnetic susceptibility (*dM/dH*)shows that *MR* of the films at low field is defined mainly by tunnelling of spin-polarized carriers between neighbouring nanometric grains.

DOI: https://doi.org/10.26799/cp-sms-nanomed-egf2019

References

1. C. Felser, L. Wollmann, S. Chadov,G. H. Fecher, *and* S. S. P. Parkin, "Basics and prospective of magnetic Heusler compounds," *APL Materials,* vol. 3, pp. 041518, 2015.
2. H. Liu, M. Tang, B. L. Guo, C. Jin, P. Li and H. L. Bai, "Effect of deposition temperature on the structure, magnetic and transport properties in Co2MnSi Heusler films," *Appl. Phys. A.*, vol. 121, pp. 141-148, 2015.
3. N. Nagaosa, J. Sinova, S. Onoda, A. H. MacDonald and N. P. Ong, "Anomalous Hall Effect, "*Rev. Mod. Phys*., vol. 82, 1539, no. 2, pp.1539-1592, 2010.
4. D. Erb, G. Nowak, k. Westerholt and H. Zabel, "Thin films of the heusler alloys Cu2MnAl and Co2MnSi: recovery of ferromagnetism via solid-state cristallization from the x-ray amorphous state, "*J. Phys. D: Appl. Phys*., vol. 43, pp. 285001-285010, 2010.
5. M. I. Youssif, A. A. Bahgat, I. A. Ali, "AC Magnetic Susceptibility Technique for the Characterization of High Temperature Superconductors, *"Egypt. J. Sol.* Vol. 23, no. 2, pp. 231-250, 2000.

Proceedings of the Joint SMS / NanoMed / EGF 2019 International Conference
Lisbon, Portugal – October 23 – 25, 2019
DOI: https://doi.org/10.26799/cp-sms-nanomed-egf2019

Tungsten Carbide Microparticles Introduction's Effect on Steel Hardness and Resistance to Local Impacts

A. Anikeev[a], I. Chumanov[b]
South Ural State University, Department of Engineering and Technology of Materials Production, Chelyabinsk, Russia
[a]anikeev-ml@mail.ru, [b]chumanoviv@susu.ru

Abstract:

The article presents one of the technological methods for producing metallic materials through the active interaction of micro- and nanoparticles in order to increase their strength characteristics. For this, based on a review of the scientific and technical literature, the technology of dispersed hardening of metal in the process of centrifugal casting is applied. To carry out disperse hardening, finely dispersed (1-5 μm) tungsten carbide particles were introduced into the metal melt during casting. The results of studies of the structure of the samples obtained using optical and electron microscopy. Tests were conducted in a laboratory setup in which steel balls with a diameter of 6 mm and a mass of 1.05 g can be accelerated to speeds of more than 600 m/s. The samples obtained, saturated with refractory microparticles of tungsten carbide, showed high hardness and resistance to local impact characteristics with a stable type of fracture.

Keywords: casting, micro and nanoparticles, tungsten carbide, crystallization, hardness, fracture.

Introduction

One of the most important tasks in metallurgy and mechanical engineering is the new materials development and their implementation, as well as material-saving technologies. Nowadays, micro- and nanocomposite materials are being used increasingly. Nanomaterials include materials containing structural elements that do not exceed 100 μm in at least one dimension and have qualitatively new properties: functional and operational. This is because the nanoelements (nanopowders, nanotubes, nanofilms) that are part of the material have large atoms fraction located on the surface. The bonds of surface atoms are partially uncompensated, which can be emerged in a number of nanoparticles' unique physical and chemical properties. New materials created using nanotechnologies or something close to them can be very useful in those industries where cost is a secondary factor, for example, in aviation, astronautics, guarding people's lives from various threats, in particular, personal protective equipment (bulletproof vests for example), designed to ensure human safety when exposed to a cold (blade) or firearms.

For successful military operations, high-strength steel may be widely considered; however, the structural steels such as low-strength steels are used in the building, automobile and industrial applications. For instance, the tallest structures are constructed using structural steel due to its constructability. High-strength and low-strength steel plates are predominantly used as civil, aerospace and military protective structures. The idea of using these plates is to protect the personnel against accidental loads, terrorist attacks or international peace keeping operations. Bhat (1985) discussed some basic principles that underlie design of materials effective for armour. The material should be able to sustain the strain gradients without cracking up. This is possible only when the ductility, which is an important quality of good armour, increases with strain rate. High hardness and impedance of the armour material can induce high stresses on the projectile which can absorb its energy on itself. Brian (1996) observed that the improved rolled homogeneous armour (IRHA) performed better than standard rolled homogeneous armour (RHA) against the L/D 5KE penetrators. Although the high hardness IRHA had more breakouts, it was still ballistically superior to old RHA steel. Buchar et al. (2002) conducted experimental and numerical studies with single and layered high-strength targets. The targets of dual hardness exhibit very good resistance against the impact of armour piercing (AP) projectile. The ballistic performance increases with the increase in the thickness of the steel with higher hardness. This is valid up to some value of this thickness. The addition of a ductile interlayer leads to the improvement in the given performance. Although the increase in the hardness of the steel improved its ballistic behaviour, the steel specimens having either 50 or 60 HRC were broken in a brittle manner rather than perforation by the projectiles (Demir et al., 2008). Hardness levels in steel plates played an important role in the ballistic performance. When the hardness of the steel plates increased, the penetration and propagation ability of the projectile decreased significantly (Übeyli et al., 2007).

DOI: https://doi.org/10.26799/cp-sms-nanomed-egf2019

Gooch et al. (2007) performed experiments using high hardness armour (HHA; 530HB) and ultra-high toughness armour (UHTA; 450HB) plates impacted by the blunt fragment simulating projectile (FSP). Two Bisalloy HHA plates were tested and both passed the requirements of MILA-46100D. It was observed that as the hardness of the steel plates increased, the ballistic limit also increased against AP projectiles. It is also noted in many instances that there is no difference in ballistic performance between UHTA and HHA, but UHTA grade is more weldable, possesses better structural properties and sometimes has more consistent ballistic performance than HHA. A detailed literature survey has been carried out on the target, and projectiles in this study have been carefully identified (Borvik et al., 2009; Dikshit, 1998; Goldsmith and Finnegan, 1986; Gupta and Madhu, 1997; Iqbal et al., 2016; Jena et al., 2010; Kilic and Ekici, 2013; Pritti et al., 1997; Showalter et al., 2007). The target material and impactor have been identified keeping in view the application in construction and automobile industry, current requirement of personnel and the lack of availability of studies in literature. The rapid technological development and increased number of wars in the 19th century led to development of sophisticated weapons. The light-weight and high-strength metals had always been the primary requirement for the weapon as well as armour industries; however, their demand increased considerably after World War II. The selection of suitable armour materials for defence applications is very crucial in order to design military vehicles, structural occupancy and military bunkers. The ideal material should possess the lowest areal density, high ductility and high strength. A number of various material systems can be considered in this perspective (Dikshit, 1998; Goldsmith and Finnegan, 1986; Gupta and Madhu, 1997; Iqbal et al., 2016; Jena et al., 2010; Kilic and Ekici, 2013; Pritti et al., 1997; Showalter et al., 2007). However, high-strength steel still seems to be an ideal material for armour applications due to high strength and superior mechanical properties. Also, the investigations on armour steel plates against normal and oblique impact by different penetrators and fragments with help of computer tool is interesting (Borvik et al., 2009; Iqbal et al., 2015, 2017).

While creating the new generation of body armor, the main parameters are the area of protection, the weight of the vest and the last one is the cost. In this regard, research aimed at reducing the products' mass while protection maintaining the level is most relevant. It should be noted that modern combined metal fabric bulletproof vests are designed based on the new concept of metal armor panel penetration with increased diameter the "plate" (spall) formation, which can be successfully stopped by a fabric bag made of special high-strength fibers. Thus, when creating new promising steel grades for the bulletproof vests manufacture, we should strive to obtain a given breakdown - spallation mechanism (Hazell, 2006).

Promising direction in the composite materials production with high mechanical characteristics could be the carbides, oxides ore nitride particles dispersion into metals (Chumanov et al., 2010; Komshukov et al., 2010).

Such materials examples are carbide steels, hard alloys, and dispersion-hardened materials (Allen et al., 2001, Kiviö et al., 2016, Watanabe et al., 2011). Dispersion-hardened materials are metal materials (mainly alloys), hardened by dispersed particles of refractory compounds (oxides, carbides, nitrides, etc.) that do not dissolve and do not coagulate in the metal matrix (base) at high operating temperatures. The maximum hardening effect is achieved with sufficiently small size of the particles in the strengthening phase (0.01-0.05 μm), their uniform distribution in the material structure and the optimal distance between the particles. To a greater or lesser extent, introduced particles interact with the melt, and the characteristics acquired by the material depend on the interaction degree, as well as on the chemical reactions products of their interaction.

One of the directions to control the dispersed particles location during metal crystallization is the disperse-hardening particles introduction into the metal during centrifugal casting (Chumanov et al., 2011). Steel and alloys used in the manufacture of machines critical parts and constructions must have fine-grained structure, as in this case they have higher complex of mechanical characteristics compared with steels having coarse-grained structure.

In this paper, we consider one of the technological methods for the metals manufacture (matrix melt) with active micro- and nanoparticles, contributing to an increase in their strength properties and a noticeable decrease in the obtaining the material cost.

Conducting experiments

Using steel mark 1020 as an example, the influence on the strength characteristics of entering into the crystallizing melt during steel casting at the centrifugal casting unit of tungsten carbide micro - and nanoparticles, was investigated. The introduced particles serve as crystallization centers, accelerate the crystallization process, grind grain and increase mechanical properties. In addition, tungsten carbide particles have high hardness; therefore, in the blanks structure, they serve as reinforcing elements that strengthen the structure. Also, to give

DOI: https://doi.org/10.26799/cp-sms-nanomed-egf2019

the experimental samples the necessary configuration, the castings forging was carried out according to the scheme proposed by the authors. This technology was taken as the basis of this work.

Samples were obtained by melting in an induction furnace, then casting was carried out in a horizontal type centrifugal casting plant, with a mold speed of 800 rpm. Casting continued for 15-20 seconds. The temperature of the metal melt was 1680-1720 °C. Reinforcing particles were introduced using a screw type dispenser. The particles size was 1-3 μm. Total 2 castings with different concentrations of reinforcing particles were obtained. Casting 1 - standard, without the dispersed particles introduction; casting 2 - with reinforcing particles concentration WC = 0.1 wt. % The resulting castings had the following dimensions: outer diameter 185 mm, inner diameter 145 mm, length 180 mm (Fig. 1).

Fig. 1 Appearance of castings

After casting, the samples were subject to deformation (forging) at the temperature of 800 °C. The scheme of samples' obtaining and deformation is shown in Fig. 2.

Fig. 2 Samples' obtaining and deformation scheme

During deformation, the wall thickness of the casting reduced from 20 mm to 5 mm. After deformation, the obtained samples were ground and polished to conduct microstructure studies using an optical and electron microscope.

Investigation of microstructure

The structure of the experimental ingots was studied using an optical microscope Axio Observer.D1m. To reveal the structure, polished samples were etched with a 5-% solution of nitric acid in alcohol. The image analysis system for metallurgical tasks and quality control "ThixometPRO" was used. From these images of the Thixomet® image analyzer, it can be concluded that all samples structure has the direction perpendicular to the forging. The structure of casting No. 1 is ferrite with small pearlite grains inclusions (Fig. 3a) located in the interdendritic gap. The structure of casting No. 2, is basically the same as in sample No. 1 (Fig. 3b), with difference in the slightly smaller size of the dendritic cell. Studies using a JEOL JSM 6460-LV electron scanning microscope made it possible to determine that the introduced WC particles are micro- and nanoscale, in some cases less than 0.5 μm (Fig. 4).

DOI: https://doi.org/10.26799/cp-sms-nanomed-egf2019

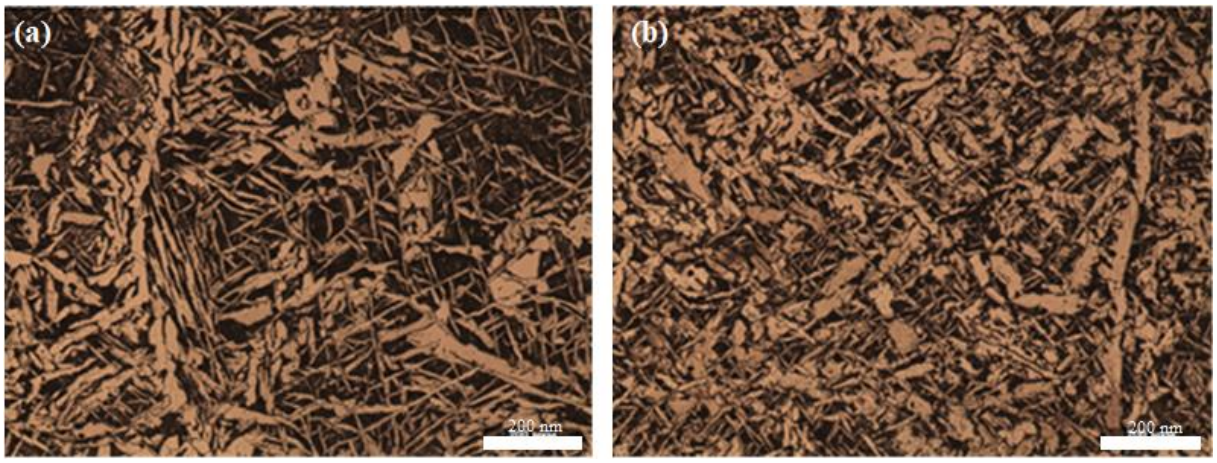

Fig. 3 Microstructure of the obtained castings: a - No. 1, b - No. 2

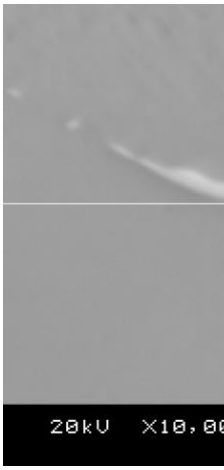

Fig. 4 WC particles in the metal structure (sample 2), × 10000

Investigation of hardness and resistance to local impacts

In order to give the samples high hardness values, normalization was carried out at the temperature of 850-870 °C. When determining Brinell hardness (HB) with a 10 mm diameter ball, a load (30 kN) was applied using an INSTRON 5882 testing machine, the load application speed was 1.25 kN/min. The prints diameters were measured in two mutually perpendicular directions using an optical microscope with 0.05 mm the division. It showed that the sample made of steel grade 20 with introduced refractory particles has a higher hardness compared to standard sample 1. Breakdown tests were carried out in a laboratory where steel balls with 6 mm diameter and 1.05 g mass can accelerate to speeds of more than 600 m/s (Sapozhnikov et al., 2013).

In this design, it is proposed to use the gases energy of standard mounting cartridges (series D and K), available on the market. The energy of these cartridges varies from 300 to 1000 J, which is quite enough to accelerate steel spherical impactors with 8 mm diameter (mass 2.2 g) with the speeds noted above. Serial production of mounting cartridges allows to obtain high stability in throwing speeds, and fixed barrel length (150 mm) - to provide compactness to the booster block and the entire stand as a whole. Mounting cartridges have lateral ignition, which requires the impact striker manufacture with needle offset from the axis by 4 mm distance. The shutter is spring, mechanical with manual cocking; the shutter can be released remotely. Since the spherical impactor has gap of about 50 μm in the barrel, it is necessary to use light wad made from polyethylene (weight about 0.25 g), which prevents the gases breakthrough into the gap and increases the coefficient of cartridge utilization energy.

Table 1 The measuring hardness results before and after heat treatment

Sample number	Diameter of the print, mm	Hardness, HB
1	5.35	129
	5.40	126
2	4.60	170
	4.55	174

DOI: https://doi.org/10.26799/cp-sms-nanomed-egf2019

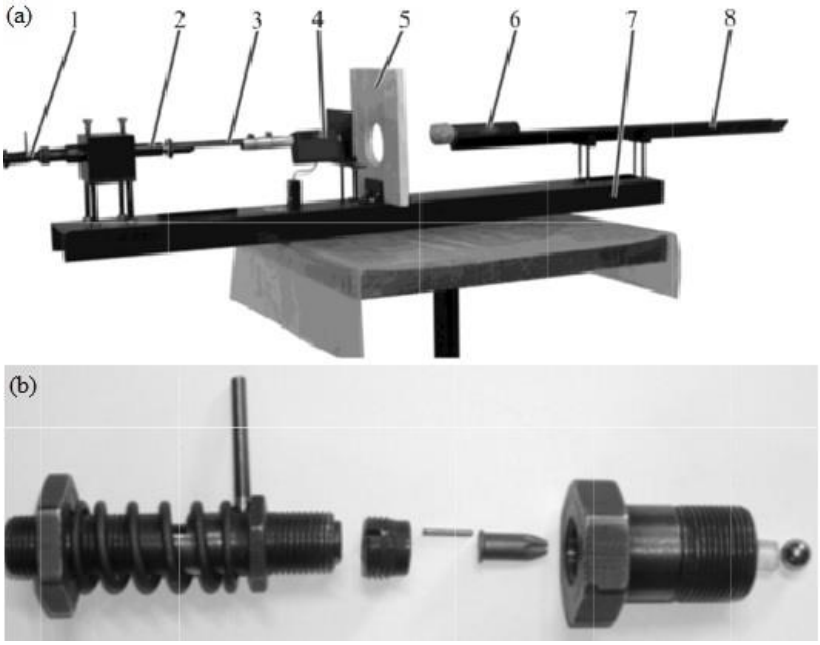

Fig. 5 Desktop overclocking stand (protective cover removed): a - 1 - shutter; 2 - trunk; 3 - gas outlet pipe; 4 - initial speed meter (chronograph); 5 - stand for the target; 6 - friction trap; 7 - base; 8 - guide traps; b - shutter and breech with wad and projectile

By changing the cartridge energy intensity or moving the wad with striker closer to the barrel cut, you can adjust the departure speed. The hammer initial velocity measurement is made by standard digital chronograph type S06 with an error of not more than 1 m/s based on 70 mm. To prevent contamination of the optical chronograph sensors by products of gunpowder incomplete combustion, the chronograph is removed from the barrel at 15 sm distance using gas exhaust tube 3. The target is set near the chronograph at 10-20 cm distance. As a result of the obstacle breakdown, the indenter speed decreases, it falls into the trap 6 , which is steel tube with fabric packing, and stops, giving it residual impulse. The trap is displaced by certain distance, overcoming the friction forces with the guide - support 8. This displacement is measured (error not more than 0.5 mm) for subsequent conversion to the striker residual velocity according to the calibration dependence. The average error in measuring the residual velocity in this way does not exceed 10 m/s (possible non-parallelism of the velocity vector v and the guide axis, friction coefficient fluctuations along the guide length, trap oscillations during movement, etc.).

Previously, special grips were developed and manufactured for fastening the studied metal samples for breakdown testing.Also, to obtain valid data, the experimental plates thickness was reduced to 2.35 mm by mechanical removal of the metal layer. This was due to the test bench design and characteristics.

The tests' parameters and the results obtained during them are presented in Table 2. During the tests, the speed of the projectile in contact with the test materials, the trap displacement, the fragments mass in the event of failure, and the breakout type were measured. The test results are presented in Fig. 6, where the numbers correspond to the test number in Table 2. According to the external evaluation of the test results, it can be noted that the refractory particles introduction into the metal matrix increases the material resistance to local impacts (in a number of tests at the same speed of the impactor breakage of plate No. 2 isn't happening).

Based on the obtained data, ballistic breakdown curves were constructed (Fig. 7), where the speed values of the steel ball are located on the abscissa axis, and the residual velocity of the tube formed as ball impact result is located on the ordinate axis.

Table 2 Initial data and experimental results

No.	Speed of projectile (m/s)	Trap offset (mm)	Mass of fragments (g)	Breakdown type
		Sample 1		
1	840	206	0.45	through
2	763	81	0.42	through
3	668	81	0.45	through
4	640	82	0.41	through
5	579	36	0.37	through
6	563	24	0.41	through
		Sample 2		
7	495	0	0.41	projectile stuck

DOI: https://doi.org/10.26799/cp-sms-nanomed-egf2019

8	571	47	0.40	through
9	466	0	-	projectile stuck
10	514	30	0.42	through
11	450	0	-	projectile stuck
12	720	84	0.44	through
13	505	0	0.44	projectile stuck

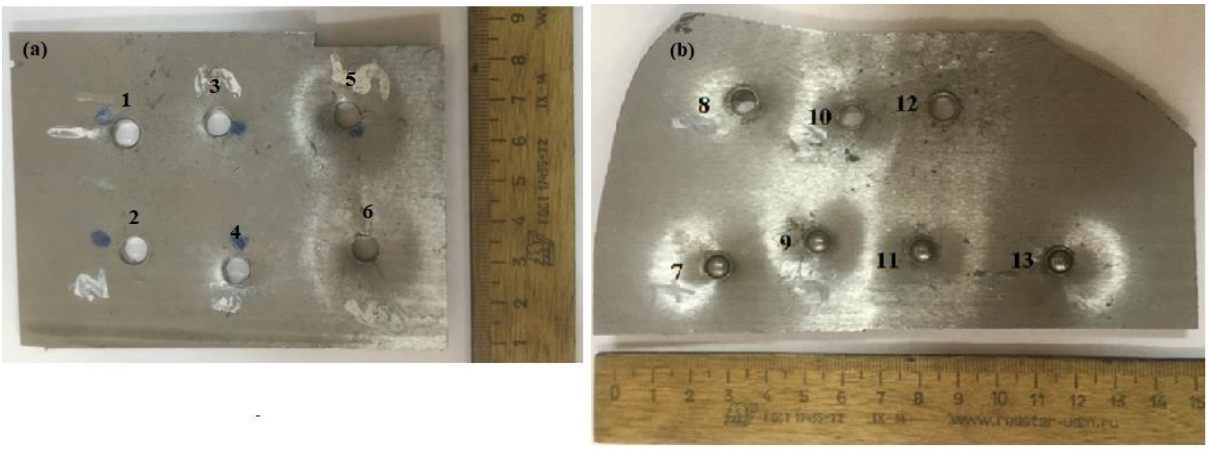

Fig. 6 Experimental samples' appearance after tests at the bench: a - No. 1, b - No. 2

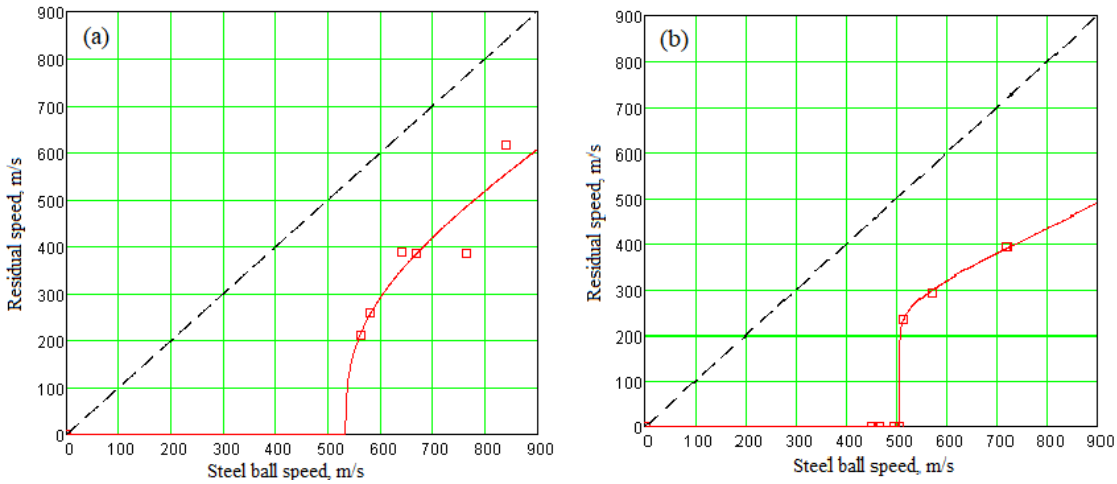

Fig. 7 Ballistic breakdown curves: a - No. 1, b - No. 2

Conclusion

When comparing the residual velocity (speed of the flying plug) with impactor speeds of 700-900 m/s in the case of a plate, which has reinforcing particles, this indicator is lower, and that indicates the increase in ballistic resistance of this material type and the resistance increase to local impacts. Thus, a sample saturated with tungsten carbide refractory microparticles has higher hardness characteristics and resistance to local impacts with a stable spall fracture type compared to ordinary steel mark 1020 sample. The results will be used in further studies, including mathematical modeling of local impact, the construction of mathematical models and testing the impact of the proposed experimental materials with firearms.

ACKNOWLEDGMENTS

This work was supported by the Ministry of Education and Science of the Russian Federation (project no. 11.9658.2017/8.9).

References

1. Allen C, Sheen M, Williams J et al. (2001) The wear of ultrafine WC-Co hard metals. Wear 250-251: 604-610. https://doi.org/10.1016/S0043-1648(01)00667-6
2. Bhat TB (1985) Science of armour materials. Def Sci J 35: 219–223.
3. Borvik T, Dey S and Clausen AH (2009) Perforation resistance of five different high-strength steel plates subjected to small-arms projectiles. Int J Impact Eng 36: 948–964. https://doi.org/10.1016/j.ijimpeng.2008.12.003
4. Brian LR (1996) Improved Rolled Homogeneous Armor (ARL-CR-285). Adelphi, MD: Army Research Laboratory.

5. Buchar J, Voldrich J, Rolc S, et al. (2002) Ballistic performance of dual hardness armour. In: Proceedings of the 20th international symposium of ballistics, Orlando, FL, 23–27 September, pp. 1–8. PA: DEStech Publications.
6. Chumanov IV, Chumanov VI and Anikeev AN (2011) Preparation of precipitation-strengthened hollow billets for rotary dispersers. Metallurgist 55(5-6): 439-443. https://doi.org/10.1007/s11015-011-9449-8
7. Chumanov VI, Chumanov IV, Anikeev AN et al. (2010) Hardening of the surface layers of a hollow billet formed by centrifugal casting. Russ Metal 2010: 1125-1128. https://doi.org/10.1134/S0036029510120104
8. Demir T, Ubeyli M and Yildirim RO (2008) Investigation on the ballistic impact behavior of various alloys against 7.62 mm armor piercing projectile. Mater Des 29: 2009–2016. https://doi.org/10.1016/j.matdes.2008.04.010
9. Dikshit SN (1998) Ballistic behaviour of thick steel armor plate under oblique impact: experimental investigation. Def Sci J 48: 271–276. https://doi.org/10.14429/dsj.48.3947
10. Goldsmith W and Finnegan SA (1986) Normal and oblique impact of cylindro-conical and cylindrical projectiles on metallic plates. Int J Impact Eng 4: 83–105.
11. Gooch WA, Showalter DD, Burkins MS, et al. (2007) Ballistic testing of Australian bisalloy steel for armor application. In: Proceedings of the 23rd international symposium on ballistics, Tarragona, 16–20 April, pp. 1181–1188. Madrid: International Ballistics Committee, Universidad Politécnica.
12. Gupta NK and Madhu V (1997) An experimental study of normal and oblique impact of hard-core projectile on single and layered plates. Int J Impact Eng 19: 395–414. https://doi.org/10.1016/S0734-743X(97)00001-8
13. Hazell PJ (2006) Ceramic Armour: Design, and Defeat Mechanisms. Argos Press, Canberra.
14. Iqbal MA, Senthil K, Bhargava P, et al. (2015) The characterization and ballistic evaluation of mild steel. Int J Impact Eng 78: 98–113. https://doi.org/10.1016/j.ijimpeng.2014.12.006
15. Iqbal MA, Senthil K, Madhu V, et al. (2017) Oblique impact on single, layered and spaced mild steel targets by 7.62 AP projectiles. Int J Impact Eng 110: 26–38.
16. Iqbal MA, Senthil K, Sharma P, et al. (2016) An investigation of constitutive behavior of Armox 500T steel and armour piercing incendiary projectile material. Int J Impact Eng 96:146–164. https://doi.org/10.1016/j.ijimpeng.2016.05.017
17. Jena PK, Mishra B, Siva Kumar K, et al. (2010) An experimental study on the ballistic impact behavior of some metallic armour materials against 7.62 mm deformable projectile. Mater Des 31: 3308–3316. https://doi.org/10.1016/j.matdes.2010.02.005
18. Kilic N and Ekici B (2013) Ballistic resistance of high hardness armor steels against 7.62 mm armor piercing ammunition. Mater Des 44: 35–48. https://doi.org/10.1016/j.matdes.2012.07.045
19. Kiviö M, Holappa L and Louhenkilpi S. (2016) Studies on interfacial phenomena in titanium carbide/liquid steel systems for development of functionally graded material. Metall Mater Trans B 47: 2114-2122. https://doi.org/10.1007/s11663-016-0658-1
20. Komshukov VP, Cherepanov AN, Protopopov EV et al. (2010) Influence of nanopowder modification of metal on the quality of continuous-cast bar. Steel Trans 40: 717-722. https://doi.org/10.3103/S0967091210080073
21. Pritti J, Castro M, Squillacioti R, et al. (1997) Improved Rolled Homogeneous Armour (IRHA) Steel through Higher Hardness (ARL-TR-1347). Adelphi, MD: Army Research Laboratory.
22. Sapozhnikov SB and Ignatova AV (2013) Experimental and theoretical investigation of deformation and fracture of subcutaneous fat under compression. Mech Compos Mater 48(6): 649-654. https://doi.org/10.1007/s11029-013-9309-7
23. Showalter DD, Gooch WA, Burkins MS, et al. (2007) Ballistic Testing of Australian Bisalloy Steel for Armour Applications (ARL-RP-181). Adelphi, MD: Army Research Laboratory.
24. Übeyli M, Yıldırım RO and Ögel B (2007) On the comparison of the ballistic performance of steel and laminated composite armors. Mater Des 27: 1257–1262. https://doi.org/10.1016/j.matdes.2005.12.005

Proceedings of the Joint SMS / NanoMed / EGF 2019 International Conference
Lisbon, Portugal – October 23 – 25, 2019
DOI: https://doi.org/10.26799/cp-sms-nanomed-egf2019

Morphology and growth of carbon nanotubes synthesis by impinging flame

L.M. Marques, A. Duarte, E.C. Fernandes
Universidade de Lisboa, Instituto Superior Técnico, IN+, Centro de Estudos em Inovação, Tecnologia e Políticas de Desenvolvimento
Avenida Rovisco Pais, 1049-001 Lisboa, Portugal,
luisamarques@tecnico.ulisboa.pt, andre.korolev.duarte@tecnico.ulisboa.pt,
edgar.fernandes@tecnico.ulisboa.pt

Abstract

In this paper, an extensive study of flame synthesis was carried out. The main objective was to understand how the production of Carbon Nanotubes (CNTs), in terms of mass, could be improved. An impinging premixed flame of Propane/Air with co-flow of Nitrogen was employed. The experiments were made at an equivalence ratio (ϕ) of 1.6 and a Reynolds number (Re) of 300 (envelope flame). The optimum height at which the substrate is placed was concluded to be at 10 mm above the burner outlet. The envelope flame mode allowed an increase of CNTs production.

Keywords: carbon nanotubes; premixed flame; impinging flame; envelope flame

1. Introduction

Carbon Nanotubes (CNTs) can be considered a rolled graphite sheet and have interesting properties which provides them various applications. CNTs exhibit semi-conducting or metallic behaviour making them terrific conductors, besides that CNTs have great flexibility, high aspect ratio, tremendous Young's modulus, large surface areas, unique combination of stiffness, strength and tenacity, very high thermal and electrical conductivity [1-2]. In result, CNTs has been considered the material of the 21st century. There are few methods known to produce CNTs, such as chemical vapor deposition, laser ablation, electric arc discharge and flame synthesis. Nevertheless, the first methods have high costs associated and/or they are time consuming. In that way, flame synthesis appears to be a solution, since it is energy efficient, cost effective, rapid, scalable and a continuous process [3]. Many types of flame configurations were used to synthesize CNTs, namely premixed flames and diffusion flames. Comparatively, premixed flames offer advantages that make them ideal for CNTs production. This type of flame promotes a rapid combustion with easily controlled flame, allowing a selection of different kinds of fuels. Besides that, it enables the adjustment of the stoichiometry of the reacting gases yielding, hence the flame chemical compositions. Temperature is also effortless adjustable, and all these aspects combined make premixed flames suitable for generation of different structures of carbon. Premixed flames are not limited by diffusion so the reactive gas profile can be made uniform by the burning system and scalability can be achieved [4]. In order to produce CNTs in a large scale, it is necessary to understand how they form and specially in which conditions the growth of CNTs is enhanced.

2. Experimental Procedure

In this experiment, it was required a Bunsen burner, mass flow controllers and the reactive gases so the desirable impinging premixed flame (Fig. 1) could be achieved. A thermocouple was implemented to analyze the temperature and a camera to capture the flame shape, as well as the depositions on the substrate (stainless steel (SS)). Throughout all the experiments the premixed flame was established by burning propane/air with co-flow of nitrogen.

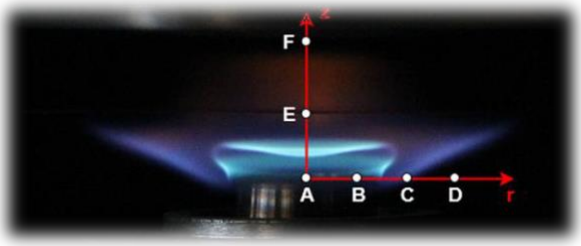

Fig. 1: Impinging premixed flame with equivalence ratio (ϕ) = 1,6 and reynolds number (Re) = 300. Coordinates (x, y) in millimeters: A = (0, 0); B = (6.5, 0); C = (13, 0); D = (19, 0); E = (0, 10); F = (0, 20).

DOI: https://doi.org/10.26799/cp-sms-nanomed-egf2019

Results and Discussion

In order to evaluate the morphology behavior over radial distance, Scanning Electron Microscopy (SEM) analysis were carried out (Fig. 2). The results showed a tendency of the diameter of CNTs decreasing from center (r = 0 mm) to end of the plate (r = 19 mm), as it is represented in Fig. 2. It can indicate that big catalytic particles are mainly located in the center of the deposition.

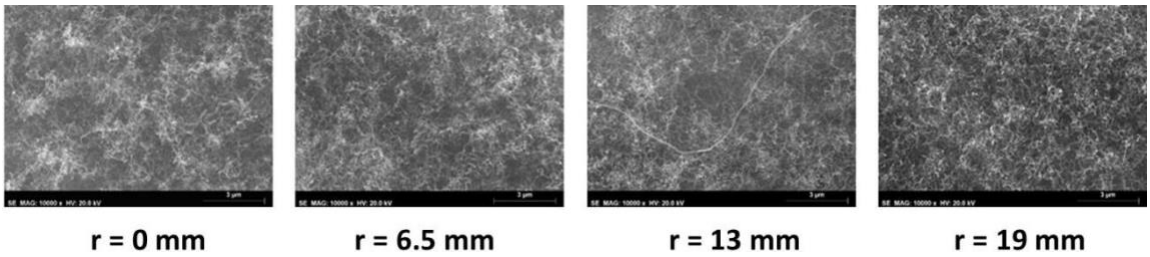

Fig. 2: SEM micrographs of CNTs over radial distance.

A mathematical model of population growth can be applied to describe the synthesis of CNTs, in terms of mass, as shown in Eq (1).

$$M(t) = \frac{M_\infty}{1 + \left(\frac{M_\infty - M_0}{M_0}\right) e^{-r_g t}} \quad (1)$$

where M_0 is the mass at the initial stage, t is the time, r_g is the mass growth rate and M_{max} is the value for which the mass produced tends as time is passing. However, when $t = 0$, M_0 is also zero and that creates an indeterminate form. In order to solve that issue, t will be substituted by $t_0 = t\text{-}t_0$, with t_0 being the first instant where mass was calculated. If logarithms are applied to Eq (1), an expression $y = ax + b$ type can be achieved, where $a = r_g$. The value of r_g can be obtained from the slope of the line and finally all the parameters are known. An average value was calculated, and a graphic evolution was obtained. Based on the experimental results, the parameters of the mathematical model were determined.

3. Conclusion

During this work, it was possible to achieve the following conclusions: (1) the envelope flame mode (Re = 300) allowed an increase of CNTs production. Combined with the substrate placed at HAB = 10 mm, the mass of CNTs synthesized was maximum and (2) it was demonstrated that temperature affects the diameter size of the CNTs obtained.

Acknowledgements

We would like to express our gratitude the IN+ and FCT for providing financial support towards FCT/MCTES (PIDDAC), (UID/EEA/50009/2013) for providing support and laboratory access to make this investigation possible.

References

1. P. M. Ajayan. “Nanotubes for carbon”, *Chemical Reviews*, vol. 99, no. 7, pp. 1787-1800, 1999.
2. Y.R. Poudel and W. Li. “Synthesis, properties, and applications of carbon nanotubes filled with foreign materials: a review,” *Materials Today Physics*, no. *7*, pp. 7-34, 2018.
3. N. Mubarak, E. Abdullah, N. Jayakumar, and J. Sahu. “An overview on methods for the production of carbon nanotubes,”
   Journal of Industrial and Engineering Chemistry, vol. 20, no. 4, pp 1186-1197, 2014.
4. S. Nakazawa, T. Yokomori, and M. Mizomoto. “Flame synthesis of carbon nanotubes in a wall stagnation flow,” *Chemical Physics Letters*, no. 403, pp. 158-162, 2005.

Proceedings of the Joint SMS / NanoMed / EGF 2019 International Conference
Lisbon, Portugal – October 23 – 25, 2019
DOI: https://doi.org/10.26799/cp-sms-nanomed-egf2019

SbSI nanowires composites for energy harvesting and sensors

Bartłomiej Toroń[1], Piotr Szperlich[1], Marcin Jesionek[1], Mateusz Kozioł[2], Marian Nowak[1]

[1] Silesian University of Technology, Institute of Physics – Center for Science and Education, Krasinskiego 8 str. 40-019 Katowice, Poland, bartlomiej.toron@polsl.pl

[2] Silesian University of Technology Faculty of Materials Engineering and Metallurgy, Krasinskiego 8 str. 40-019 Katowice, Poland, mateusz.koziol@polsl.pl

Abstract

Composites containing antimony sulfoiodide (SbSI) nanowires have found application in the production of nanogenerators and nanosensors. Due to high values of electromechanical coefficient (k_{33}=0.9) and piezoelectric coefficient ($d_{33}=1\cdot10^{-9}$ C/N), SbSI is a very attractive material for such devices. SbSI nanowires have lateral dimensions 10–100 nm and length up to several micrometers. They are sonochemically produced. This work presents a few various nanocomposites: production methods, their properties, and examples of application. A piezoelectric paper based on SbSI nanowires is reported. The composite of tough SbSI nanowires with very flexible cellulose leads to applicable, elastic material suitable to use in fabrication of, for example, piezoelectric nanogenerators. Fabrication technology of epoxy resin/SbSI nanowires composite is also presented. In this case nanowires have been added to epoxy resin in mass ratio 1:4, and then ultrasound irradiation has been used for homogenization of the mixture. This nanocomposite has also been used to fabricate a deformation sensor integrated into an FRP (fiber reinforced polymer) laminate structure. These sensors are also presented in this work. The sensors were made from a nanocomposite based on epoxy resin and SbSI nanowires. Performed electrical measurements show that it is possible to determine the laminate deformation as a function of registered voltage.

Keywords: SbSI nanowires, nanocomposites, nanogenerators, nanosensors, energy harvesting, FRP laminates

1. Introduction

In this paper fabrication technologies of cellulose/SbSI nanowires composite (CSNC), epoxy resin/SbSI nanowires composite (ESNC), and FRP laminate based on ESNC have been presented. The first report of the synthesis of antimony sulfoiodide (SbSI) was given by Henry and Garot in 1824 [1]. In 1958 E. Mooser and W.B. Person predicted the semiconducting properties of $A^{15}B^{16}C^{17}$ compounds [2]. The intensive investigation of SbSI started in the early 60ies by R. Nitsche, W. J. Merz [3], and E. Fatuzzo et al. [4] who discovered its photoconductivity, piezoelectricity, and ferroelectricity. The antimony sufoiodide is one of the best piezoelectric materials with high volume piezoelectric modulus $d_{33}=1\cdot10^{-9}$ C/N [5] and electromechanical coupling coefficient k_{33}=0.90 [6] in case of single crystals. Due to these properties, SbSI is used for nanogenerators and nanosensors [7-10].

Presented nanogenerators were tested on a vibration plate with a frequency of 24 Hz for various load resistances. The FRP sensors were tested for various deflection speeds (in the range 1-300 mm/s) and for constant deflection x=1 mm. Vibrations within the frequency range 1-150Hz are the most useful due to the fact their common occurrence in human-environment i.e. vacuum cleaners, refrigerators, clothes dryers, washing machines. The fabricated FRP laminates with an integrated sensor can be used to monitor i.e. construction condition.

In this paper, we present the fabrication method of the mentioned composites and preliminary results of energy harvesting (in the mentioned region of low-frequency vibration) and sensor technology. Moreover, the composite is easy and cheap in production.

2. Materials and Methods

2.1. Materials

The SbSI nanowires were prepared from the constituents (the elements: antimony, sulfur, and iodine), weighed in the stoichiometric ratio: 1.843 g Sb, 0.485 g S and 1.921 g I. All used reagents were of analytical purity. The elemental mixture was immersed at room temperature and ambient pressure in ethanol, which was contained in a closed polypropylene container to avoid outflow of volatile synthesis products. The cylinder was partly submerged in water in a cup-horn of 750 Watt ultrasonic processor VCX-750 equipped with sealed converter

DOI: https://doi.org/10.26799/cp-sms-nanomed-egf2019

VC-334 (Sonics & Materials, Inc.). The frequency of ultrasound was 20 kHz and intensity was over 550 W/cm^2. The constant temperature of water (293 K) was kept during the whole process. During the sonification, a sol was formed. When the sonification process was finished, a red-orange gel with an absorption edge of SbSI clearly identified was obtained. The gel was then rinsed with pure ethanol to remove remaining substrates and centrifuged to extract the product. Then SbSI gel was dried under 60 Pa pressure at room temperature. Prepared xerogel consisted of SbSI nanowires with lateral dimensions 10 nm to 100 nm and length up to several micrometers. The SEM image of obtained xerogel consisted of SbSI nanowires is shown in Fig 1.Chemical route of SbSI nanowires growth and details of the morphology, crystallographic structure, and chemical composition of the sonochemically produced SbSI xerogel have been presented in [11, 12].

A piezoelectric paper based on SbSI nanowires is reported. The composite of tough SbSI nanowires with very flexible cellulose leads to applicable, elastic material suitable to use in fabrication of, for example, piezoelectric nanogenerators. Piece of Northern Bleached Softwood Kraft (NBSK) was used as a source of cellulose. NBSK was comminuted by high energy ultrasounds using the VCX-750 ultrasonic processor. The sonication was continued to receive single cellulose fibers dispersed in water. Then SbSI nanowires were added to cellulose fibers in the mass ratio 1:4. Ultrasound irradiation was used again to ensure a homogeneous mixture of cellulose fibers and SbSI nanowires. The dilute suspension of CSNC was deposited on blotting paper and the rest of the water was eliminated by pressing.

Fabrication technology of epoxy resin/SbSI nanowires composite is also presented. In this case, nanowires have been added to epoxy resin in the same mass ratio as in the case of CSNC, and then ultrasound irradiation has been used for homogenization of the mixture. This nanocomposite has also been used to fabricate a deformation sensor integrated into an FRP (fiber reinforced polymer) laminate structure. These sensors are also presented in this work. The sensors were made from a nanocomposite based on epoxy resin and SbSI nanowires. Performed electrical measurements show that it is possible to determine the laminate deformation as a function of registered voltage. The scheme of fabrication methodology is shown in Fig. 1. More detailed information one can find in [7, 9, 13].

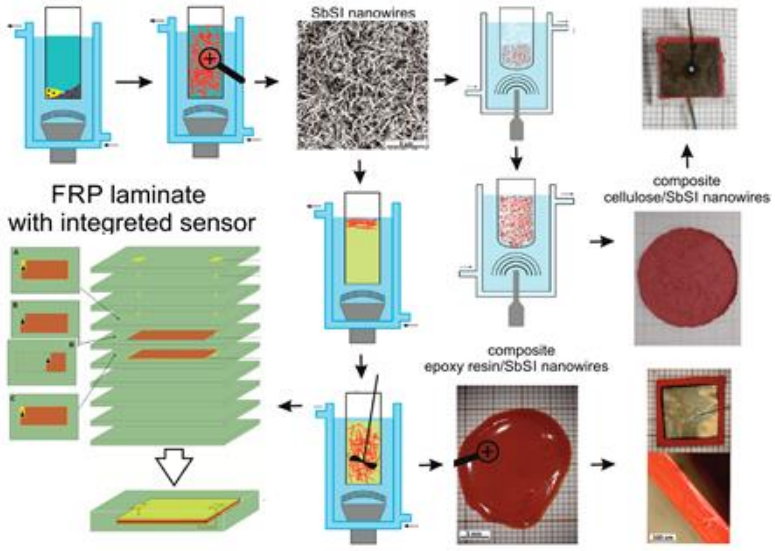

Fig. 1. Scheme of sonochemical preparation of SbSI nanowires, the ESNC and CSNC, generator/sensor assembly and scheme of FRP laminate with integrated sensor [7, 9, 13]. Description in the text.

2.1. Methods

CSNC and ESNC samples were mounted on a plexiglass plate attached to a vibration generator to measure the piezoelectric properties. The frequency and amplitude of vibration were measured by vibrometer WH-30 equipped with octave filter FO-1. Measurements of U-I characteristics for different load resistances were performed using the Zeal decade resistance box (1 Ω – 1 GΩ). The output voltage was recorded using EG&G 5110 dual-phase lock-in amplifier.

3-point non-destructive bending tests were performed in order to evaluate the piezoelectric properties of the manufactured FRP laminate sensors. The tests were carried out using the INSTRON 4469 machine. The sample was bent at a constant speed of the loading bar to a deflection of 1.0 mm. The tests were carried out for the

DOI: https://doi.org/10.26799/cp-sms-nanomed-egf2019

loading bar speed at 1, 2, 5, 10, 20, 40, 60, 80, 100, 150, and 300 mm/min. The electric response of the sample was continuously measured during the test using a Keithley 6517A electrometer. During the nondestructive deflection, the load-deflection curves were recorded.

3. Results

Figure 2 shows the comparison of U-I characteristics under vibration excitation for different load resistances for CSNC (a) and ESNC composite (b). In the case of the ESNC, the results for two different nanowires content (20 % and 40 %) in the composite are compared. One can notice two facts. First of all, the signal registered for CSNC is almost ten times smaller than in the case of ESNC. Secondly, the response of ESNC nanogenerator with increased needle content (40 %,●) is smaller (U=25 mV) than with fewer SbSI nanowires in the composite (20 %,●, U=45 mV). It is associated with the agglomeration of SbSI nanowires, appearing for their higher content in the composite. SEM micrograph showed that 20 % SbSI nanowires content in composite does not cause their agglomeration, while this phenomenon can be observed in the case of samples containing 40 % SbSI nanowires.

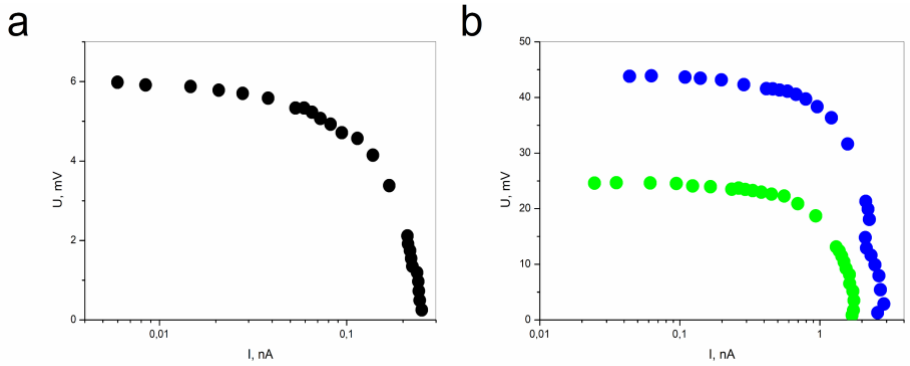

Fig. 2. Comparison of U-I characteristics recorded under vibration excitation (f=24 Hz, A=1mm) for different load resistances for CSNC (a) and for ESNC (b) with 40% (●) and 20 % (●) concentration of SbSI nanowires.

Electrical results registered for FRP laminates with integrated sensors on the base of ESNC are presented in figure 3. Presented voltage values were recorded during reloading (fig. 3a) and loading (fig. 3b) of samples. Black and red points represent the results for various SbSI nanowire concentrations in the sensor layer (■ - 40 %, ■ - 20 %). One can see that the character of changes is the same for both contents of SbSI nanowires in the sensor layer, while the piezoelectric response of the FRP laminate sample with 20% of SbSI nanowires weight concentration is almost ten times higher than for the one with 40% of SbSI nanowires concentration. Since ESNC composite was used as the sensor layer, this phenomenon can be caused by the aforementioned agglomeration.

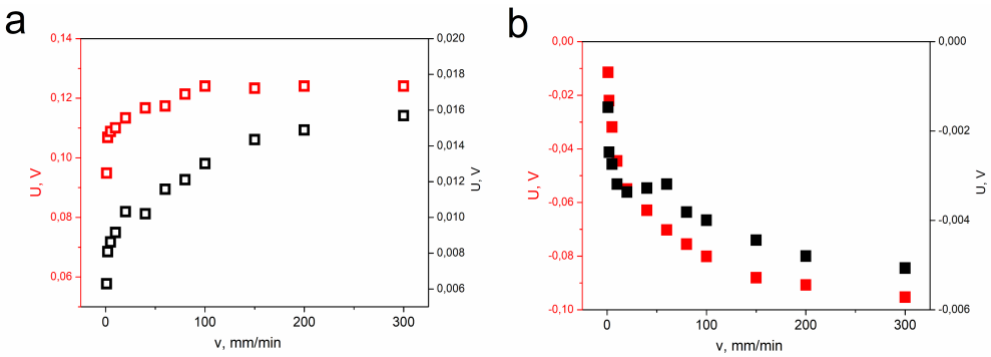

Fig. 3. Determined values of maximum voltage for different speed of deformation and constant value of maximum deflection (x=1 mm) during loading (a) and reloading (b). Black and red colors correspond to 40% and 20 % concentration of SbSI nanowires in ESNC, respectively.

4. Conclusion

The presented paper shows the comparison of piezoelectric response for vibration excitation (f=24 Hz, A=1mm) for various load resistances for CSNC (fig. 2a) and for ESNC (fig. 2b) with 20% and 40 % concentration of SbSI nanowires. Analyzing fig . 2 one can notice that matrix material has a significant influence on the piezoelectric properties of the composite. Moreover, a comparison of registered results for ESNC with various amount of

DOI: https://doi.org/10.26799/cp-sms-nanomed-egf2019

nano-additive leads to a conclusion, that the increase of a volume fraction of SbSI nanowires leads to decreasing of the output signal. It can be caused by the agglomeration of SbSI nanowires.
In the case of FRP laminate, the increase in SbSI nanowires mass fraction from 20% to 40% may cause a decrease in FRP laminate mechanical response. It requires further studies.

Acknowledgments

The study is financially supported by the Silesian University of Technology in the frame of grants: BKM507/RIF2019.

References

1. H. Garot, "D'un produit résultant de l'action réciproque du sulfure d'antimoine et de l'iode," *Journal de Pharmacie,* vol. 10, pp. 511-524, 1824.
2. E. Mooser, W. B. Person, "The crystal structure and properties of the group VB to VIIB elements and the compounds formed between them," *J. Phys. Chem. Solids,* vol. 7, pp. 65-77, 1958.
3. R.Nitsche, W. J. Merz, „Photoconduction in ternary V-VI-VII compounds," *J. Phys. Chem. Solids,* vol. 13, pp. 154-155, 1960.
4. E. Fatuzzo, G. Harbeke, W. J. Merz, R. Nitsche, H. Roetschi, W. Ruppel, "Ferroelectricity in SbSI," *Physical Review,* vol. 127, pp. 2036-2037, 1962.
5. A. A. Grekov, S. P. Danilova, P. L. Zaks, V. V. Kulieva, L. A. Rubanov, L. N. Syrkin, N. P. Chekhunova, A. M. Elgard, "Piezoelectric elements made from antimony sulphoiodide crystals," *Akusticheskii Zurnal,* vol. 19, pp. 622-623, 1973.
6. K. Hamano, T. Nakamura, Y. Ishibashi, T. Ooyane, "Piezoelectric property of SbSI single crystal," *J. Phys. Soc. Japan,* vol. 20, pp. 1886-1887, 1965.
7. M. Kozioł, B. Toroń, P. Szperlich, M. Jesionek, "Fabrication of piezoelectric strain sensor based on SbSI nanowires as a structural element of a FRP laminate," *Composites Part B,* vol. 157, pp. 58-65, 2019.
8. K. Mistewicz, M. Nowak, R. Paszkiewicz, A. Guiseppi-Elie, "SbSI nanosensors: from gel to single nanowire devices," *Nanoscale Research Letters,* vol. 12, pp. 97 1-8, 2017.
9. B. Toroń, P.Szperlich, M. Nowak, D. Stróż, T. Rzychoń "Novel piezoelectric paper based on SbSI nanowires," *Cellulose,* vol. 25, pp. 7-15, 2018.
10. K. Mistewicz, M. Nowak, D. Stróz, R. Paszkiewicz, "SbSI nanowires for ferroelectric generators operating under shock pressure," *Materials Letters,* vol. 180, pp. 15-18, 2016.
11. M. Nowak, „Photoferroelectric nanowires," in *Nanowires Science and Technology,* N. Lupu, Ed. Rijeka: Intech, 2010, pp. 269-308.
12. M. Nowak, P. Szperlich, Ł. Bober, J. Szala, G. Moskal, D. Stróż, „Sonochemical preparation of SbSI gel," *Ultrason. Sonochem.,* vol. 15, pp. 709-716, 2018.
13. P. Szperlich, B. Toroń An ultrasonic fabrication method for epoxy resin/SbSI nanowire composites, and their application in nanosensors and nanogenerators," *Polymers,* vol. 11, pp. 479 1-13, 2019.

Proceedings of the Joint SMS / NanoMed / EGF 2019 International Conference
Lisbon, Portugal – October 23 – 25, 2019
DOI: https://doi.org/10.26799/cp-sms-nanomed-egf2019

Analysis of various Aspects in Metals Creation with Given Microheterogeneity Degree

A. Anikeev,[1] I. Chumanov[1]

[1] South Ural State University, Department of Engineering and Technology of Materials Production, Chelyabinsk, Russia

Abstract:

The article discusses various aspects of the metals creation with given microheterogeneity degree, obtained by introducing dispersed particles into the melt. When creating such materials, it is important to take into account many aspects: the conditions for the dispersed particles separation from supersaturated solution, the particles interaction level with metal, the feed rate to the melt, distribution control, the particles number in the melt volume, the microheterogeneity influence on the properties' level, and other aspects. The article analyzes modern approaches for solving each aspect, proposes the methodology for calculating the crystallization rate and particle distribution when fed into the metal during centrifugal casting. Based on the developed methodology, computer model was built allowing to predict the particles distribution depending on many factors.

Keywords: dispersed particles, cast alloys, wetting, injection rate, microheterogeneity, distribution density

Given the finiteness of natural resources and the new challenges posed by the technology development, the materials creation with given properties level, while reducing cost is the most important task of our time. One of the solutions to this problem can be economically alloyed metals with given microheterogeneity degree. Microheterogeneity can be obtained by introducing carbides, oxides, or nitrides dispersed particles (or isolating them from supersaturated solution) and their predetermined distribution in the volumes that are most affected. The low cost of the resulting material is due to the fact that the main material (matrix) volume can consist of carbon steel, inexpensive steel, and a high level of mechanical characteristics in surface volumes is achieved by creating microheterogeneity.

When creating materials with given microheterogeneity degree, scientists face various problems:

1. the difference in the microparticles densities and the melt (uncontrolled uneven distribution);
2. microparticles interaction with metal (wetting level);
3. predicting the micro-particles distribution by the melt volume;
4. The microheterogeneity effect on properties level.

For controlled particles sedimentation in the melt by specific gravity, some researchers have proposed the method of introducing dispersed particles into the melt when casting on centrifugal casting machine. In this case, particles with density greater than or equal to the melt density under the centrifugal forces action move to the external volumes of the centrifugal cast billets. Particles with density lower than that in the material, with certain density difference, under the Archimedean forces influence move into the workpiece inner layers. By changing various casting parameters (workpiece size, volume and the supplied particles dispersion, crystallization rate, etc.), it is possible to obtain material with a given microheterogeneity degree [1, 2].

To study the wetting dispersed metal particles parameters, leading research laboratories apply the still drop techniques and capillary technique. The distinctive feature in the second method is the high accuracy corresponding to real conditions. In this technique, the particles under investigation and the metal wetting them are heated in separate chambers, and the liquid metal is deposited on particles substrate. This technique has already shown impressive results in number of studies, proving its accuracy [3-5].There are several mathematical models for prediction of the particles distribution by volume, in the world at the moment. Most of them are based on the steady state assumption: models describing the criteria for dropping particles by a growing crystallization front [6], models calculating the critical particle absorption rates by growing dendrites crystals [7].

Some models attempt to describe the system dynamic state [8] or to determine the criterion for capturing non-metallic inclusions by the solidification front during centrifugal metal casting [9]. Some researchers use existing models not to predict the introduced particles distribution, but to more efficiently remove existing oxide particles from the metal and increase its properties [10, 11].

Based on existing models, the article's authors developed mathematical and computer model of the particles distribution over the metal volume during centrifugal casting. The model takes into account various parameters: casting temperature, workpiece size, volume fraction and dispersion of particles, crystallization rate and others. The computer model was developed on the"Ansys 16.0" basis and allows predicting the dispersed particles input distribution in real conditions with a high degree of accuracy (Fig. 1, 2).

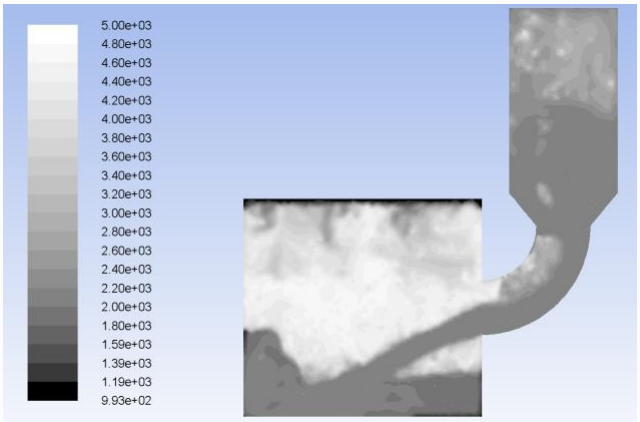

Figure 1: Modeling the temperature fields distribution during casting.

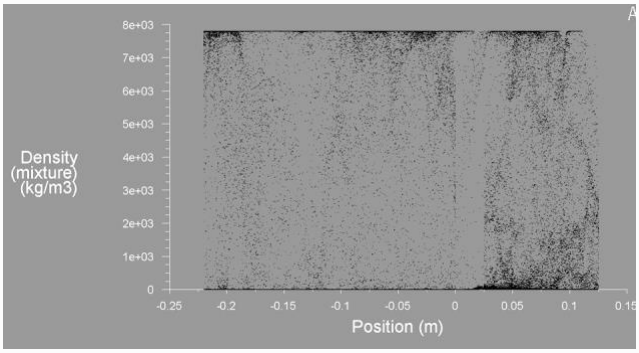

Figure 2: Particle distribution diagram on the horizontal axis.

The introduced particles have significant effect on the metal properties. This is achieved by increasing the crystallization rate, particles incorporation into the crystal lattice and the "reinforcement" effect. The particles influence degree on the mechanical properties is determined by several factors: the metal chemical composition, the introduced particles type and dispersion, and the density of particles distribution in the crystallized metal volume [12].

An advantage of the particle distribution method is the ability to obtain various mechanical properties in single material without an obvious phase boundary (as is the case with coatings). Thus, the introduction of 3.6 % of tungsten carbide dispersed particles allows to increase the mechanical properties of low carbon steel, to increase the tensile strength by 36-38 %, impact strength by 23-26 % and wear resistance by 29-34 %. This approach feature is that when using different class steel (for example, stainless steels), the introduction effect will be different [13-15].

Thus, the article analyzes various aspects of creating metals with given microheterogeneity degree obtained by introducing dispersed particles into the melt, and modern approaches to solving each of the aspects. The computer model has been developed that has great application possibilities for materials with given microheterogeneity degree. This materials' class is one of the most promising, since it allows to significantly increase properties only in given volumes, reducing the scarce alloying elements consumption.

References:

1. Watanabe, Y., Sato, H. (2011), Review Fabrication of Functionally Graded Materials under a Centrifugal Force, *in book "Nanocomposites with Unique Properties and Applications in Medicine and Industry" (ed. by John Cuppoletti, InTech)*, 372-378.

2. Chumanov, I., Anikeev, A. (2015), Fabrication of functionally graded materials by introducing wolframium carbide dispersed particles during centrifugal casting and examination of FGM's structure, *Procedia Engineering*, 2, 816-820.
3. Kiviö, M., Holappa, M., Yoshikawa, T. (2012), Interfacial Phenomena in Fe-TiC Systems and the Effect of Cr and Ni, *High Temp. Mater. Processes*, 31(4-5), 645-656.
4. Sobczak, N., Nowak, R., Radziwill, W. (2008) Experimental complex for investigations of high-temperature behaviour of molten metals in contact with refractory materials, *Mater. Sci. Eng., A*, 495(1-2), 43-49.
5. Kiviö, M., Holappa, L., Louhenkilpi S. (2016), Studies on interfacial phenomena in titanium carbide/liquid steel systems for development of functionally graded material, *Metall. Mater. Trans. B*, 47, 2114-2122.
6. Han, Q., Hunt, D. (1995), Particle pushing: critical flow rate required to put particles into motion, *J. Cryst. Growth*, 152(3), 221-227.
7. Wilde G., Perepezko H. (2000), Experimental study of particle incorporation during dendritic solidification, Mater. Sci. Eng., A, 283(1-2), 25-37.
8. Catalina, A., Mukherjee, S., Stefanedcu, D. (2000), A dynamic model for the interaction between a solid particle and an advancing solid/liquid interface, *Metall. Mater. Trans. A*, 31(10), 2559-2568.
9. Wang, Q., Zhang, L. (2016), Determination for the Entrapment Criterion of Non-metallic Inclusions by the Solidification Front During Steel Centrifugal Continuous Casting, *Metall. Mater. Trans. B*, 31 (10), 1933-1949.
10. Wang, Q., Zhang, L. (2016), Detection of Non-metallic Inclusions in Centrifugal Continuous Casting Steel Billets, *Metall. Mater. Trans. B*, 47(3), 1594-1612.
11. Martinez, E., Peaslee, D., Lekakh, S. (2011), Calcium Wire Ladle Treatment to Improve Cleanliness of Centrifugally Cast Steel, *Transactions of American Foundry Society*, 119, 513-520.
12. Türker, M., Çapan, L. (2017), Effect of inclusions on mechanical properties of Nb stabilized austenitic stainless steels (316Nb) with centrifugal and sand casting techniques, *Matériaux et Techniques,* 105(3), #2017035.
13. Anikeev, A., Seduhin, V., Sergeev, D. (2016), Increase in wear resistance by introduction of titanium carbide dispersed particles, *Mater. Sci. Forum*, 843, 269-273.
14. Al-Mangour, B. Grzesiak, D. (2016), Selective laser melting of TiC reinforced 316L stainless steel matrix nanocomposites: Influence of starting TiC particle size and volume content, *Mater.Des.*, 104, 141-151.
15. Li, H., Li, P., Chen, W. (2017), Effect of WC and Co on the microstructure and properties of TiC steel-bonded carbide, *Mater. Sci. Forum*, 898, 1468-1477.

Acknowledgments
This work was supported by the Ministry of Education and Science of the Russian Federation (project no. 11.9658.2017/8.9).

Proceedings of the Joint SMS / NanoMed / EGF 2019 International Conference
Lisbon, Portugal – October 23 – 25, 2019
DOI: https://doi.org/10.26799/cp-sms-nanomed-egf2019

Ca 2p Photoelectron Spectroscopy of Cortical and Subchondral Femoral Bone Tissue in Intact and Damaged Areas

X.O. Brykalova[1], N.N. Kornilov[2], A.A. Pavlychev[1*]
[1] St.Petersburg State University, Department of Physics,
Peterhof, Saint Petersburg, RF. xenia.olegovna@gmail.com
[*]andrey.pavlychev@gmail.com
[2] Vreden Russian Research Institute of Traumatology and Orthopedics,
Saint Petersburg, RF. drkornilov@hotmail.com

Abstract

Bone is one of the most complicated hierarchically organized material in nature. X-ray photoelectron spectroscopy (XPS) provides a sensitive evaluation of relationships between hierarchical organization of bone and its local electronic and atomic structure. In this study XPS is used to investigate proximal side of cortex and subchondral bone in intact and osteoarthritis damaged knee compartments. The medial and lateral condyles of the femur resected during total knee arthroplasty in patients with medial compartmental knee osteoarthritis were used as samples. The methods for the bone samples preparation are discussed. The Ca $2p_{3/2,1/2}$ binding energy and full-width-at-half-maximum of the Ca $2p_{3/2,1/2}$ photoelectron lines are obtained for the proximal sides of rat cortex and femur bone cuts. The distal side of the cuts are also examined. The difference between the spectroscopic characteristics of Ca^{2+} 2p excited healthy and arthritic areas is revealed and examined within the original 3DSL model. Perspectives for development of novel methods for medical imaging and diagnosis of subchondral bone at subcellular level are discussed.

Keywords: hierarchical matter, electronic and atomic structure of bone, cartilage - bone interface, Ca 2p binding energy, osteoarthritis, X-ray photoelectron spectroscopy

1. Introduction

Bone is the most intriguing hierarchically organized and multilevel structured matter. In modern medicine, the problems originated from skeletal pathology are of great socio-economic importance associated primarily with economic costs directed to medical treatment, rehabilitation and care of patients with osteoarthritis and the consequences of osteoporosis. Osteoarthritis is the fourth most common cause of hospitalization. Annual costs, according to various estimates range from 3.4 up to $ 60 billion, which is associated only with medical care (51%) and a decrease in productivity (49%) [1].

Material science, biological and medical research discloses the complex hierarchy of the skeleton designs from macro- to nanolevels. Specifically, nanolevel studies of bones encounter great difficulty mainly because electronic and atomic structure as well as molecular architecture of their nanoblocks are not fully understood. This gap prevents from successful solution of many fundamental and clinically relevant problems such as the development of new methods of medical imaging at subcellular levels and medical diagnosis of skeletal pathology at early stage. The morphological models [2-9] based on ideas concerning the structural and functional organization of the skeleton in the normal and pathological conditions describe peculiarities of skeletal structural organization and its functional properties. The predominantly qualitative character of these models does not allow their quantitative checking at nanoscale. Elaboration of quantitative ex- and in-vivo models of bone tissue and their comprehensive verification by applying modern experimental techniques is a key problem for medicine and materials science.

X-ray photoelectron spectroscopy (XPS) is a prospective tool to extract quantitative information about electronic and atomic structure of native bone and its interaction with cartilage in joints and to develop new methods for medical imaging and diagnosis of bone at subcellular level. In addition the investigations of molecular architecture of native bone will enable us to determine optimal conditions for its self-healing. Apart of the medical aspects the investigations favor for developing of cutting-edge nanotechnologies and for bio-designing of smart materials [9].

How is the local electronic and atomic structure as well as molecular architecture of bone material distorted in case of skeletal pathology? Recently the 3D super lattice model (3DSL) model was suggested [10] to answer this

DOI: https://doi.org/10.26799/cp-sms-nanomed-egf2019

question and describe local electronic and atomic structure of bone tissue. This model takes into account the structure-functional organization of the skeleton and the peculiarities of electron waves propagation in 3D superlattice assembled from the nanocrystallites of hydroxyapatite $Ca_{10}(PO_4)_6(OH)_2$ (NHAPs). In accord with the model the distinct HAP-to-bone changes are revealed in the Ca^{2+} 2p-, P 2p- and O 1s near edge X-ray absorption fine structure (NEXAFS) spectra [10 - 12]. These spectral changes serve to visualize the effect of high hierarchical levels on electronic and atomic structure of HAP crystal.

In the work we focus on age- and arthritis-related changes in local electronic and atomic structure of bone tissues. Our main objective is to reveal the changes by examining the Ca^{2+} $2p^{-1}$ photoelectron (PE) lines in cortical bone of young, adult and mature rats as well as subchondral bone in intact and pathology damaged area by comparing them with the reference spectra of HAP. It is known that skeletal pathology leads to distortions in electronic and atomic structure of bone. In particular, it results in site-dependent changes in crystallinity, binding energy and chemical composition of bone in healthy and osteoarthritic (OA) damaged knee compartments [13]. In the paper we focus on deviations between age- and arthritis-related changes in energy positions and Gaussian widths of the Ca $2p_{3/2,1/2}^{-1}$ PE lines. These spectral changes are discussed in the framework of the 3DSL model. It is stated that appearance of new non-apatitic components in the Ca^{2+} $2p_{3/2}^{-1}$ and Ca^{2+} $2p_{1/2}^{-1}$ PE lines specifies the main distortions in electronic and atomic structure in OA damaged area. The origin of these non-apatitic components is discussed and assigned with the distortions of electronic and atomic structure in damaged knee compartments. We have assumed that it is the coupling of mineralized phase with erased cartilage that results in the spectral changes.

2. The 3DSL model

The 3DSL model suggested in [10] gives a key for understanding of basic relationships between hierarchical organization of the skeleton and local electronic and atomic structure of mineralized bone. According to [10] the effective NHAP can be presented as a rectangular block with dimensions $\langle L_x \rangle \times \langle L_y \rangle \times \langle L_z \rangle \approx$ 20×7,5×3,5 nm^3. It contains about $40 \cdot 10^3$ atoms. These blocks are separated one from other by the hydrated layer with the thickness $\langle d \rangle \approx 2$ nm. The coplanar assembly of the crystallites is described as a superperiodic lattice with the basic vectors of translation $\mathbf{b}_j = \mathbf{L}_j + d$, where $\mathbf{L}_j = \langle L_j \rangle \vec{j}$ and $\vec{j}$ is the unit vector in Cartesian coordinates. Considering NHAP as an extended crystallographic cell derived in such a way that their coplanar assembly would form a single-crystal HAP in case the separating layers disappear. In the assumptions the electronic structure of the 3D superlattice is approaching to the band structure of HAP when $\langle d \rangle \to 0$.

This approximation is a suitable platform for investigations of HAP-to-bone deviations at subcellular level. According to the 3DSL model the band structure of bone obeys the Heine equation [10**,** 14]

$$X_j^2(k) - 2Z(E)X_j(k) + 1 = 0\,. \tag{1}$$

Here $X_j(k) \equiv e^{i\vec{k}\vec{b}_j}$. The coefficient $Z(E)$ links the band dispersion $E(k)$ with the short-, long-range and super-order parameters of mineralized bone:

$$Z(E) = \mathrm{Re}(T(E;\langle d \rangle, \langle L \rangle_j)^{-1}\,. \tag{2}$$

$T(E;\langle d \rangle,\langle L \rangle)$ is the amplitude of electron transmission through the supercell, where $\langle d \rangle$ is the averaged thickness of the hydrated nanolayer and $\langle L \rangle$ is the averaged size of NHAP. T is tightly related with the amplitudes T' and T'' of waves transmitted through and the amplitudes B' and B'' of waves reflected from the NHAP and the hydrated layer, respectively. Eq. 1 assigns the certain energy E with the wave number k. Solving this equation we derive

$$|\,\delta E_{core}\,| << \delta E_{val,n} \approx 2E_n \langle d \rangle \Big/ \langle L \rangle\,. \tag{3}$$

DOI: https://doi.org/10.26799/cp-sms-nanomed-egf2019

The inequality is obtained in suppositions (i) $|B'B''|<<1$ for the red shift ΔE_{val} of valence bands and (ii) $|T'T''|<<1$ for the shift ΔE_{core} of a core bands in bone. The red shift ΔE_{val} is discussed in more detail in the work [10, 11]. En is the n-band energy in the single HAP crystal. Thus, Eq. 3 shows that the mechanism related with super periodicity of mineral matrix produces minor shift of the Ca 2p band compared to valence bands in bone.

3. Experimental data

To study local electronic and atomic structure in healthy and OA damaged areas XPS techniques is applied. The XPS spectra of HAP and bone are measured by using the photoelectron spectrometer Thermo Fisher Scientific Escalab 250Xi. The Ca $2p_{3/2,1/2}^{-1}$ PE lines are obtained from proximal side of the bone samples. Just for comparison XPS measurements of HAP are carried out too. To investigate subchondral bone in intact and damaged areas the medial and lateral condyles of the femur resected during total knee arthroplasty in patients with medial compartmental knee OA are used as samples. Figure 1 displays the knee joint affected by OA and appearance of the intact and damaged (sclerotic) areas indicated by arrows. The bone sample of damaged bone is a saw cut of the femoral condyle, subjected to excessive mechanical stress due to the development of arthritis and deformity in the joint, with full-layer loss of cartilage. The sample of healthy bone is a saw cut of the condyle of the same femoral bone, not subjected to excessive load, with intact cartilage. The bone samples are prepared in Vreden Russian Research Institute of Traumatology and Orthopedics.

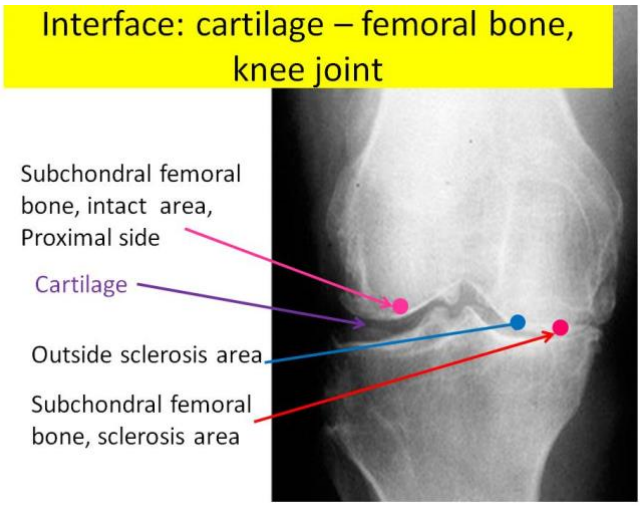

Fig. 1: Arrows point on the sclerotic and intact areas on proximal side of femoral bone, the region outside the sclerotic area is also shown.

3.1. Samples

Powdered bone and synthetic HAP samples were used as objects. The HAP of almost stoichiometric composition (a = 9.416 (2), c = 6.880 (1)) was synthesized by applying the reverse precipitation method in an ammonium-containing solution as it is described in [11]. The cortical bone samples are prepared from middle third of the femur, tibia and humorous white mongrel young, adult and mature male rats. Cortex has been (i) thoroughly cleaned of soft tissue, (ii) washed in saline, (iii) dried with blotting paper, and (iv) grinded to fine powder with particles of size 1 mkm.

Two samples preparation methods for the XPS measurements were used. The first [13]: the bone saw cuts were cleaned of cartilage tissue using a gentle mechanical treatment with a scalpel, to subchondral bone plate. Then, to degrease the cuts and delete the myeloid contents from the trabeculae of the spongy layer, the samples were kept for 4 days in a bath with an aqueous 33% hydrogen peroxide solution (H_2O_2) mixed in a 1:1 ratio with hot water (60° C) and with the addition of 5 ml of 10% aqueous ammonium hydroxide solution (NH_4OH). This mixture was replaced daily. To complete the cleaning process the samples were placed for one day in distilled water, changing it every 6 hours. To depress the intercrystallite water evaporation the samples were subjected to heating at 200°C for 2 days in thermostat. The second preparation method consisted in cleaning of cartilage tissue with a scalpel and subsequent lyophilization of the bone samples followed by their heating at 180° C for two days.

Before the PE measurements the argon-ions-cleaning of the samples was used. These methods were applied respectively to the samples. Note that in contrast to cortex additional thermal treatment of subchondral bone is required to depress the water evaporation from the samples.

3.2. Experimental data analysis and discussion

Skeletal pathology affects local electronic and atomic structure and molecular architecture of mineral matrix in bone tissue attracts our attention. Recently the site-dependence of cristallinity, binding energies and composition of sunchondral bone in intact and damaged knee compartments were detected in [13] by applying X-ray diffraction and XPS techniques to medial and lateral condyles of the femoral bone resected during total knee arthroplasty in patients. The authors [13] have observed the change in crystallinity varying from 28% in intact to 38% in sclerotic area on the proximal side. Specifically the change in crystallinity is not observed on their distal side. The HAP-to-bone red shifts of the Ca 2p binding energy and broadening of the Ca $2p^{-1}$ PE lines was tentatively attributed to the contribution of amorphous calcium phosphate [13]. The authors [13] have suggested a change in chemical bonding and the formation of new molecular-like compounds on surface inside the sclerotic area.

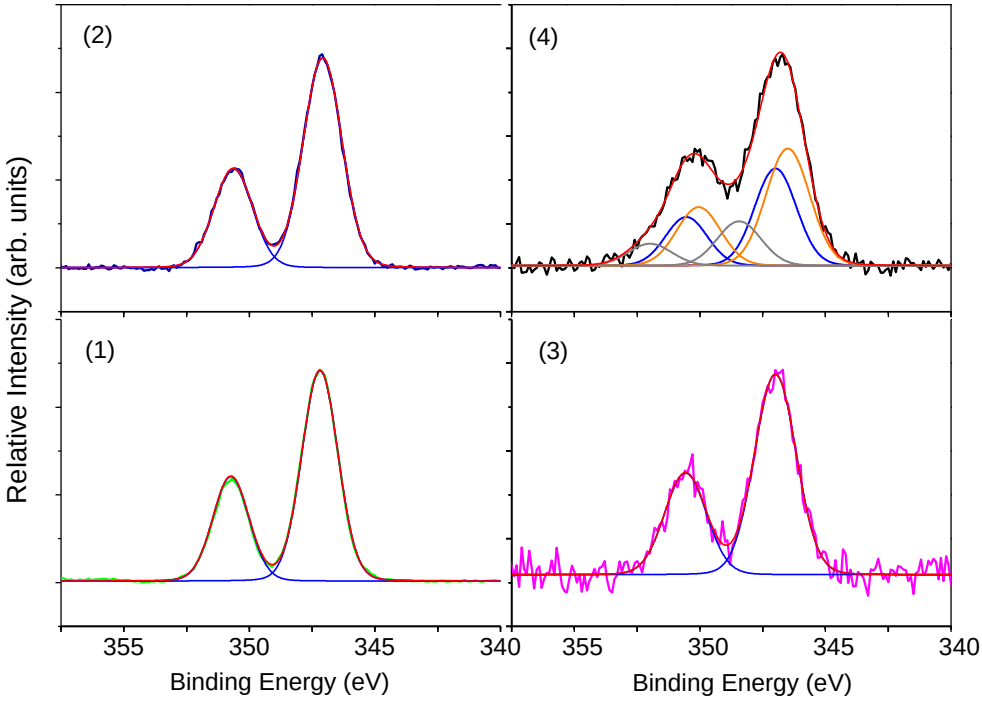

Fig. 2: The experimental Ca $2p_{3/2,1/2}^{-1}$ PE lines in HAP (1), mature rat cortical bone (2), healthy subchondral bone (3) and subchondral bone in sclerotic area (4). The de-convoluted spin-orbit splitting of the Ca $2p_{3/2,1/2}$ ionized states are also shown with solid lines. Panel 4: A, B and C-components are shown with blue, orange and grey, respectively.

DOI: https://doi.org/10.26799/cp-sms-nanomed-egf2019

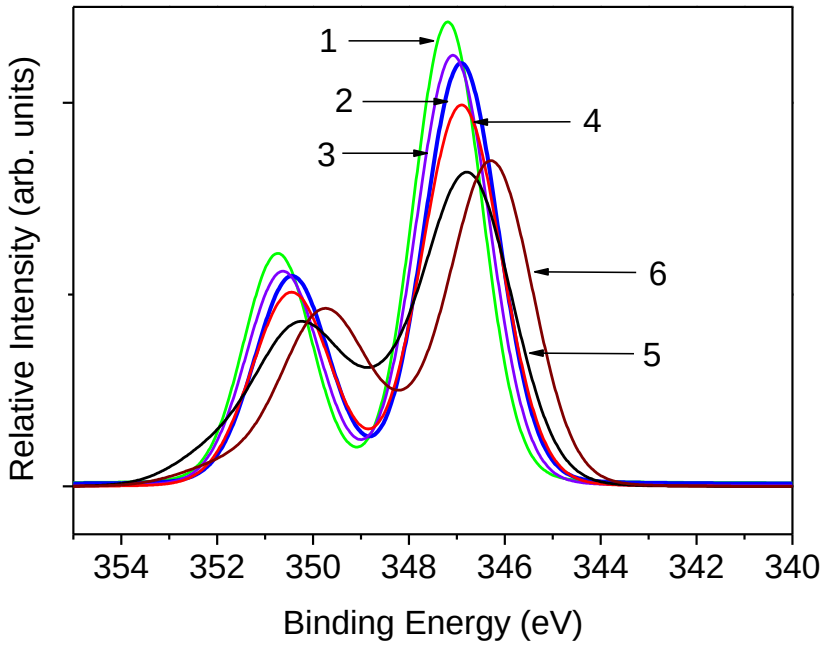

Fig. 3: Ca $2p_{3/2}^{-1}$ ad $2p_{1/2}^{-1}$ PE lines measured in the work. 1 – HAP (green line), 2 and 3 - cortex of young (blue) and mature rats (violet), 4 and 5 subchondral bone in intact (red) and sclerotic areas (black line), 6 - subchondral bone outside the sclerotic area (dark red).

Table 1: Spectral positions, Lorentzial and Gaussian widths of the Ca $2p_{3/2,1/2}^{-1}$ PE lines in HAP, cortex of young, and mature rats as well as subchondral bone in the different areas. The values are in eV. The relative intensities of the A, B, C components are also shown.

Phase	Ca $2p_{3/2}$ BE (WFHM)	HAP-to-bone red shift(broadening)	Ca $2p_{1/2}$ BE (WFHM)
HAP	A-comp 347.2 (1.6)		A-comp 350.75 (1.6)
Cortex, young rats	A-comp 346.9 (1.8)	0.3(0.2)	A-comp 350.45 (1.8)
Cortex, mature rats	A-comp 347.1 (1.8)	0.1(0.2)	A-comp 350.65 (1.8)
Subchondral, #1, intact	A-comp 347.0 (1.9)	0.2	A-comp 350.55 (2.0)
Subchondral, #1, sclerotic	A-comp 347.0 (1.9) B-comp 346.5 (2.0) C-comp 348.4 (2.0) A/B = 0.79; A/C=2.3	0.2(0.3)	A-comp 350.55 (1.9) B-comp 350.05 (2.0) C-comp 351.95 (2.0)
Subchondral, #1, outside sclerotic area	A-comp 347.0 1.9 B-comp 346.2 1.9 C-comp 348.4 2.0 A/B = 0.15, A/C =1.2	0.2(0.3)	A-comp 350.55 (1.9) B-comp 349.75 (1.9) C-comp 351.95 (2.0)

The measured Ca $2p_{3/2,1/2}^{-1}$ PE lines in HAP, young rat cortex, healthy and sclerotic areas of subchondral femoral bone are plotted in Fig. 2. The reference binding energies of the Ca $2p_{3/2}$ and Ca $2p_{1/2}$ levels in HAP are found equal to 347.2 eV and 350.75 eV. These values are in good agreement with the energies obtained by Eighmy and co-authors [15]. Comparing them with the binding energies in bone tissues we see the distinct HAP-to-bone red shift and broadening of the Ca $2p_{3/2}^{-1}$ and Ca $2p_{1/2}^{-1}$ PE lines. In bone they are shift towards low binding energies

DOI: https://doi.org/10.26799/cp-sms-nanomed-egf2019

about 0.1 - 0.3 eV and broadened ≤0.4 eV compared to HAP. To document the HAP-to-bone changes the Ca $2p_{3/2,1/2}^{-1}$ PE lines are fitted by using Voigt functions. The best fitting results are exhibited in the Fig. 2.

One may see that the complex composition of the spin-orbit Ca $2p_{3/2}$ and Ca $2p_{1/2}$ components is observed only in the sclerotic area. The extracted spectroscopic parameters of the core-ionized HAP and bone tissues are collected in Table. Our analysis of the experimental Ca $2p_{3/2}^{-1}$ and Ca $2p_{1/2}^{-1}$ PE line shapes allows us to assign the A- and B-component with "apatitic" and "quasi-calcite" states, respectively. The assignment of the C requires further investigations.

To highlight the HAP-to-bone spectral changes the measured XPS data are normalized to the total intensity of the Ca $2p_{3/2}^{-1}$ and Ca $2p_{1/2}^{-1}$ PE lines and compared in Fig. 3. The distinct differences in the PE lines are clear visible. The influence of the different sample preparation methods on electronic and atomic structure of subchondral bone is discussed.

4. Conclusion

It is stated that the age-related changes in XPS spectra of cortex are tightly connected with the red shift of the Ca^{2+} 2p binding energy which decreases from young to mature bone. Only a single "apatitic" component dominates in the Ca^{2+} $2p_{3/2}^{-1}$ and Ca^{2+} $2p_{1/2}^{-1}$ PE line shapes. It is stated that appearance of non-apatitic components specifies the substantial changes in electronic and atomic structure in OA damaged area of subchondral femoral bone. The contribution of the non-apatitic components strongly increases outside the sclerotic area. The distortions of electronic and atomic structure in OA damaged knee compartments are regarded to be closely connected with interaction of NHAPs and erased cartilage. The obtained results indicate the directions for development of novel approaches to medical imaging and diagnosis of bone tissue at subcellular level and innovational technologies in medical treatment.

Acknowledgements

The XPS study was carried out with the support of the St. Petersburg State University Resource Centres "Centre for Physical Methods of Surface Investigation", and "Centre for Diagnostics of Functional Materials for Medicine, Pharmacology and Nanoelectronics". The work is supported by RFBR grant number 19-02-00891

References

1. B. Yucesoy, L.E. Charles, B. Baker and C.M. Burchfie, "Occupational and genetic risk factors for osteoarthritis: A review", *Work*, vol. 50, no. 2, pp. 261–273, 2015.
2. W.F. Neuman and M.W. Neuman, *The chemical dynamics of bone mineral*, Chicago: University of Chicago Press, 1958.
3. J. Currey, *The mechanical adaptation of bones*, Princeton, NJ: Princeton University Press, 1984.
4. S. Weiner and H.D. Wagner, "The material bone: Structure-mechanical function relations", *Annu. Rev. Mater. Sci.*, vol. 28, pp. 271-298, 1998
5. Y.I. Denisov-Nikolski, S.P. Mironov and N.P. Omeljanenko, *Actual problems of theoretical and clinical osteoartrology*, Moscow: Novosti, 2005. [in Rus]
6. B.A. Zhilkin, Y.I. Denisov-Nikolski and A.A. Doktorov, "Structural organization and formation of cortical bone", *Uspekhi sovremennoy biologii* [*Advance in modern biology*] vol. 123, no. 6, pp. 590-598, 2003. [in Rus]
7. A.S. Avrunin, R.M. Tikhilov, I. I. Shubniakov, L.A. Parshin, B.E. Melnikov and D.G. Pliev, "Hierarchy of spiral organization of skeletal structures. Interrelationship between structure and functions", *Morfologiia [Morphology]*, vol. 137, no.2, pp. 69-75, 2010. [in Rus]
8. A.S. Avrunin, R.M. Tikhilov, A.B. Abolin and I.G. Shcherback, "Levels of bone mineral matrix organization and the mechanisms determining parameters of its formation", *Morfologiia [Morphology]*, vol. 127, no. 2, pp. 78-82, 2005. [in Rus]
9. M. Buehler, "Molecular nanomechanics of nascent bone: fibrillar toughening by mineralization", *Nanotechnology*, vol. 18, pp. 295102-295110, 2007.
10. A.A. Pavlychev, A.S. Avrunin, A.S. Vinogradov, E.O. Filatova, A.A. Doctorov, Y.S. Krivosenko, D.O. Samoilenko, G.I. Svirskiy, A.S. Konashuk and D.A. Rostov, "Local electronic structure and nanolevel hirarchical organization of bone tissue: theory and NEXAFS study", *Nanotechnology*, vol. 27, 504002, 2016.

DOI: https://doi.org/10.26799/cp-sms-nanomed-egf2019

11. A.S. Konashuk, D.O. Samoilenko, A.Y. Klyushin, G.I. Svirskiy, S.S. Sakhonenko, X.O. Brykalova, M.A. Kuz'mina, E.O. Filatova, A.S. Vinogradov and A.A. Pavlychev, "Thermal changes in young and mature bone nanostructure probed with Ca 2p excitations", *Biomed. Phys. Eng. Express*, vol. 4, 035031, 2018.
12. J. Rajendran, S. Gialanella and P.B. Aswath, "XANES analysis of dried and calcined bones", *Science and Engineering C*, vol. 33, pp. 3968-3679, 2013.
13. X.O. Brykalova, N.N. Kornilov, A.A. Cherny, Y.A. Rykov and A.A. Pavlychev, "Electronic and atomic structure of subchondral femoral bone in intact and osteoarthritic knee compartments", *Eur. Phys. J. D.*, vol. 73, 113, 2019.
14. V. Heine, "The pseudopotential concept", *Solid State Physics. Advance in Research and Applications*, vol. 24, pp. 1-36, 1970
15. T. Taylor Eighmy, A. E. Kinner, E.L.Shaw, J.D. Euksden and C.A. Francis, "Hydroxylapatite ($Ca_5(PO_4)_3OH$) characterization by XPS: An environmentally important secondary mineral", *Surface Sci Spectra*, vol. 6, pp. 193-201, 1999.

Proceedings of the Joint SMS / NanoMed / EGF 2019 International Conference
Lisbon, Portugal – October 23 – 25, 2019
DOI: https://doi.org/10.26799/cp-sms-nanomed-egf2019

The next generation of Smart Textiles

K.M.B. Jansen
Delft University of Technology
Landbergstraat 15, Delft, The Netherlands, k.m.b.jansen@tudelft.nl

Abstract

Smart Textiles are garments with integrated sensors and actuators which can be used to measure bodily conditions (like hearth rate, sweating and muscle activity), posture, localized body movements as well as touch and pressure. They can be regarded as a new application field for microelectronic devices. The smart textiles field largely benefits from a series of recent developments: sensors become smaller, more reliable and require less power and, on the other hand, energy harvesting techniques are continuously improving as well as energy storage devices like flexible batteries and super capacitors. Based on these rapid developments it is not unlikely to expect that in the near future we indeed will have textiles with an integrated battery less sensor network which will continuously monitor the health of patients, soldiers or you yourself.

Notwithstanding these optimistic prospectives, it must be realized that smart textiles have been a promise for already two decades and are still not really emerging in the markets. In this paper we will discuss the developments and trends, list the challenges and propose a strategy to come to The next Generation of Smart Textiles.

Keywords: Smart Textiles, wearables, sensors, flexible electronics

1. Introduction

According to the IdTechEx report [1] the market for e-textiles is currently close to the $100m in annual wholesale revenue and is expected to grow towards the $5 bn in 2027. The key market sectors include Sports & Fit-ness, Medical & Healthcare, Wellness, Home & Lifestyle, Military, Fashion and Automotive. This rapid growth and spreading over the different market sectors is quite fascinating and calls for a more in depth study on how the sectors of electronics and textiles could merge towards a novel market field.

When discussing market trends however care should be taken to discern between wearables and smart textiles (electronics textiles, e-textiles). Wearables are rigid electronic devices like the Fitbit with strongly integrated sensors, electronics and power supply which are worn on or close to the body. Smart textiles on the other hand have a similar strong integration of sensors, electronics and power supply as wearables but in addition are soft and seamlessly integrated in textile products. In addition, for smart textiles to be accepted in our society they should have all the properties similar to what we expect for normal clothing: they should be stretchable, washable, durable as well as unobtrusive to wear. This means that where wearables can be developed and produced by the electronics industry itself, for smart textiles an intensive collaboration between the electronics industry and the textile industry is unavoidable. Sensors must be made flexible and with low energy consumption but should also be able to connect and seamlessly integrated in the garments in a way that complies with the mass manufacturing processes used in the textile industry. It is clear that all of these demands result in a series of challenges to deal with. The above reasons will undoubtedly contribute to the explanation for the discrepancy between the huge potential of electronic textiles and the fact that after 10 to 20 years of development there is hardly any penetration to the market yet. Smart textiles in fact seem to follow the Gartner hype cycle [2] and are currently in the through of disillusionment (Figure 1).

In the sections below we discuss what can be done to move forwards to a future where smart textiles become an accepted part of our way of living.

DOI: https://doi.org/10.26799/cp-sms-nanomed-egf2019

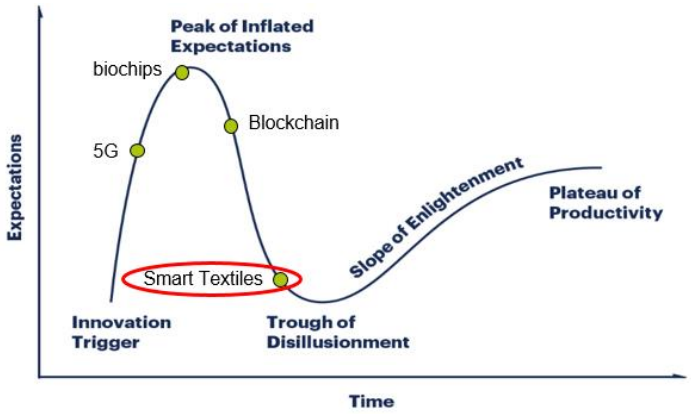

Fig. 1: Gartners hype cycle for Smart Textiles [2]

2. Textile based sensors

The simplest way to add interaction and intelligence to garments is to use commercially available off-the-shelf actuators (LEDs, buzzers, etc) and sensors (to measure e.g. stretch, bending, hearth rate, temperature, ECG) and focus on the interconnection and integration. Such sensors are rigid and need special protection to withstand machine washing which, in the end, often makes the sensor system bulky and uncomfortable. Philosophizing about a future generation of sensors which are completely unobtrusive, it is clear that these sensors must be soft, stretchable and conformable to the human body as well as that they must be breathable, robust and washable. One way to achieve this is by introducing flexibility and stretchability in the circuit board and electronics [3]. In this way the integration of the polymeric or rubbery sensor substrate with the textile based fabric still may cause durability problems (sensor delamination, interconnect problems). An interesting alternative seems to use textile based sensors which have the potential to be seamlessly integrated in garments. Studies in this direction involve the work on embroidered fabric keyboards of Post [4], Mattana's work on woven temperature and humidity sensors [5] and of course the Google Jacquard project [6].

In the Emerging Materials lab in Delft we developed textile based sensors for measuring local stretch and body posture. The starting point was to use commercially available stretchable fabrics like Silverell, MedTex, LessEMF or StretchFabric as well as non-stretchable conductive yarns and fabrics to construct simple deformation or pressure sensors. This can be done by e.g. monitoring changes in resistance or capacity during stretching and optimizing the sensor layout. An example of such simple textile based stretch sensors is shown in Figure 2a [7]. Problems that we encountered were the signal decay after a stretch and the signal response due to both stretch and pressure. The latter was significantly improved by constructing a capacity type sensor with interdigit electrodes and embedding it in a thin layer of silicon rubber (utmost right sample in Figure 2a). A much more robust and washable textile stretch sensor is shown in figure 2b. The sensors consist of two conductive, non-stretchable fabrics which were attached to stretchable non-conductive fabrics in such a way that upon stretching the electrode overlapping area increased, resulting in a measurable change in capacitance [8]. The fitness shirt in which these sensors are implemented is shown in Figure 3, right.

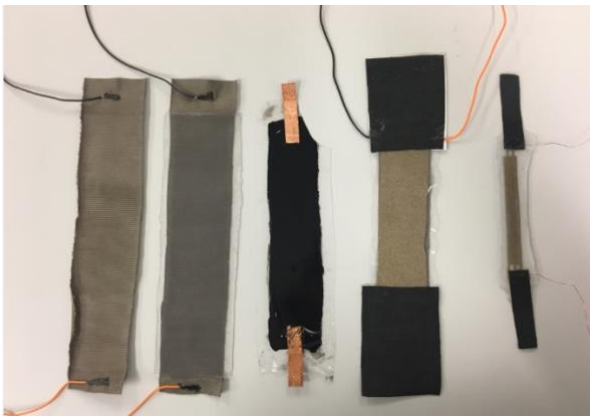

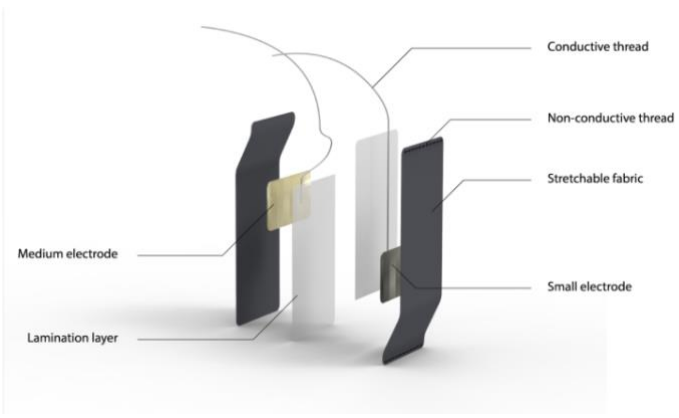

Figure 2a) textile based soft stretch sensors [7]; b) Washable textile based stretch sensor [8]

DOI: https://doi.org/10.26799/cp-sms-nanomed-egf2019

Figure 3: Examples of smart textile prototypes. Left a stress monitoring vest with off-the-shelf, rigid sensors and copper interconnection wires; Right a posture monitoring fitness shirt with textile based sensors [8]

Although the above samples are promising examples of soft, textile based sensors, they all are still add on sensors and are not yet completely integrated in the garment. Such a seamless integration could for example be obtained by constructing sensors from knitted conductive yarns into the fabric. By varying the intra line spacing and pattern of those conductive traces areas can be created in which the capacity change during deformation can serve as a stretch indicator. Such sensor areas will have the same thickness and stretchability as the surrounding fabric and will thus be truly unobtrusive.

3. Integrated textile circuitry

In current smart textile prototypes all sensors, power and data transfer units are usually still connected by copper wiring. This wiring is non-stretchable and sometimes hidden in an extra layer of textile which may affect the comfort. More important is that all this external wiring is not compatible with the current large scale textile production processes. This in fact may be one of the main reasons that currently only a very small portion of all the bright ideas for smart textile products could make the step to a profitable commercial product.

The best way to deal with this is to integrate the wiring in the garment itself. In that way it can be easily mass produced by the textile industry after which the sensor and data processing units should be added (either by hand, or automated). This idea is similar to how electronic components are interconnected by mounting them on a so-called printed circuit board (PCB). Li and Tao [9] therefore introduced the term Fabric Circuit Board (FCB). The idea of integrating conducting wires in textiles with the aim to create a wearable, textile data network probably goes back to the works of Gorlick [10] and Post et al. [4]. Gorlick prototyped elastic suspenders with embedded copper wiring onto which batteries and sensors could be connected with especially designed connectors. Post, on the other hand, used conductive yarns and an embroidery machine to create sensors and interconnect a series of electronic components in textiles [4]. Amongst the applications they show are the Firefly dress and the Musical Jacket with a fabric keypad. Later on other researchers followed up. Park et al. introduced the idea of a wearable motherboard with ribbon cables and snap fitting pin connectors [11], whereas Li and Tao used knitted copper wires and a helical spring connection to the sensor elements [9].

4. Proposal for a modular smart textile system

In section 2 we discussed the option of developing soft or textile based sensors but is good to realize that this will not be possible for all sensors and actuators and that we still have to deal with the integration of hard or partly flexible sensor modules in the garment. This can be done by gluing or sewing the casing onto the textile layers and soldering the interconnections or by inserting the modules in specially prepared pockets. The current situation is that in each smart garment project a different approach is used. We therefore propose here to develop a single modular smart textile system with a standard interconnect technology for mounting the sensor modules, power units and data processing nodes to the fabric circuit board mentioned above. A schematic example is shown in Figure 4.

DOI: https://doi.org/10.26799/cp-sms-nanomed-egf2019

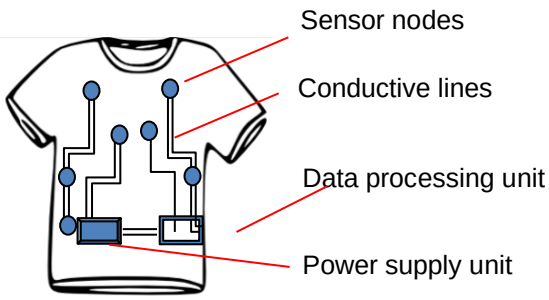

Figure 4: Modular Smart Textile system

Such a modular smart textile system will have a series of advantages. First of all, the textile part of the garment (including the interconnects) can be manufactured with the standard mass production techniques of the textile industry whereas the sensor and data processing units (with the other half of the standardized interconnection) can be separately manufactured by the electronics industry without the need for intensive contact to discuss the way of interconnecting. The sensor and other external units can then be connected later by the end user when receiving the smart garment package. An additional advantage is that malfunctioning or outdated sensor modules can be simply replaced individually without the need to discard the entire garment. Changing, updating or adding sensors can then be done in a similar way as we currently work with apps on our mobile phones. Moreover, with such a garment the electronic components can be easily separated from the textile part at the end-of-life.

The main challenge to solve then is how to develop and standardize these interconnects between the soft garment fabric and the more rigid external modules. In the past already a number of possibilities has been proposed like click or snap fit connections, magnetic connections [8], sewing, using conductive glue or soldering [6]. Important is that the interconnections are robust, reliable, easy to attach and de-attach and, above all, standardized. In order to achieve this we need a joint effort between representatives of both the textile and the electronics industry to select, test, develop and standardize the interconnect technology.

4. Conclusion

In this paper we discuss and suggest several options to come to a new way of designing and manufacturing smart textile systems which are soft and unobtrusive to wear, robust and washable and can easily be mass manufactured. First of all we suggest to develop and use conductive yarns and fabrics to fabricate soft and textile based sensors for a number of relatively simple sensing function (e.g. to monitor local stretch and pressure variations or to detect touch based on capacity changes). Furthermore we propose to use a modular setup in which all the wiring is integrated in the garment and external sensor and data processing units can be interconnected using a yet to be developed and standardized technology.

With all this we can imagine that in a not too distant future we can select a smart (fitness) shirt with our own preferences for colour, shape and design and with our own selection of sensor units. After the ordering the smart fitness shirt package will arrive at home, we can snap on the sensor units, activate the app and start using it. If we want to update or add an extra sensor we can simply order it and add to our shirt. In such a scenario people will probably order more than one of those shirts and transfer the sensor units from one shirt to the other with a few clicks such that the shirts can be properly cleaned if needed (although washing with attached sensors is of course also possible). With a joint effort of both the textile and the electronics industries we expect smart textiles to emerge on the market soon.

References

1. https://www.idtechex.com/research/reports/e-textiles-2017-2027-technologies-markets-players-000522.asp
2. https://www.gartner.com/en/research/methodologies/gartner-hype-cycle
3. M. Gonzalez et al., Design and implementation of flexible and stretchable systems, *Microelectronics Reliability* 51, 2011, pp.1069-1076
4. E.R. Post et al., E-broidery: Design and fabrication of textile-based computing, *IBM Systems J*. 39, 2000, pp.840-860

5. G. Mattana et al., *IEEE Sensors Journal* 13, 2013, pp.3901-3909
6. I. Poupyrev et al., Project Jacquard: Interactive digital textiles at scale. In: *CHI '16*, 2016, 4216-4227
7. E. Fridriksdottir, Soft and stretchable sensors for on-the-body strain sensing, Internship report Delft University of Technology, 2018
8. R. Schevers, Smart Sportswear: wearable feedback on sports performance, Graduation report Delft University of Technology, 2016
9. Q. Li and X. M. Tao, Three-dimensionally deformable, highly stretchable, permeable, durable and washable Fabric Circuit Boards, *Proc. R. Soc*. A 470: 20140472, 2014
10. M.M. Gorlick, Electric suspenders: a fabric power bus and data network for wearable digital devices, *Wearable Computers*, 1999, pp.114-121
11. S. Park et al., The wearable motherboard: A framework for personalized mobile information processing (PMIP), *Design Automation Conf. Proc*., 2002, pp.170-174